Tectonophysics 892 (2024) 230531

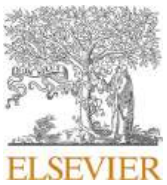

Contents lists available at ScienceDirect

Tectonophysics

journal homepage: www.elsevier.com/locate/tecto

Crustal imaging and characterization of active faults with a large-N nodal deployment - Application to the Chaînons Béarnais region (western Pyrenees foothills, France)

Sébastien Chevrot [a,*], Matthieu Sylvander [b], Nicolas Saspiturry [c], Amine Ourabah [d], Sébastien Benahmed [b], Benoît Derode [e], Frank Grimaud [b], Jean Letort [b], Hélène Pauchet [b], Guy Sénéchal [f], Antonio Villaseñor [g], Jean-Baptiste Ammirati [a]

[a] GET, UMR 5563, Observatoire Midi Pyrénées, Université Paul Sabatier, CNRS, IRD, Toulouse, France
[b] IRAP, UMR 5577, Observatoire Midi Pyrénées, Université Paul Sabatier, CNRS, Toulouse, France
[c] Géosciences Montpellier, Université de Montpellier, CNRS, Montpellier, France
[d] Stryde, 1-2 Paris Garden, London SE1 8ND, United Kingdom
[e] ITES, UMR 7063, École et Observatoire des Sciences de la Terre, Université de Strasbourg, CNRS, Strasbourg, France
[f] Université de Pau et des Pays de l'Adour, LFCR, E2S-UPPA, CNRS, Pau, France
[g] Institute of Marine Sciences (ICM), CSIC, Barcelona, Spain

ARTICLE INFO

Keywords:
Pyrenees
Active faults
Local earthquake tomography
Earthquake location

ABSTRACT

Understanding the driving forces and nature of intraplate seismicity remains a major unsolved problem in seismology. In the western Pyrénées, seismicity is concentrated in a narrow region that follows the boundary between the Axial Zone and the North Pyrenean Zone. Despite the presence of a permanent network in the region, the geometry of active faults, and their relationship with crustal structures, remain elusive, owing to significant earthquake location uncertainties. Here, we exploit data recorded by a large-N nodal array deployed in the Chaînons Béarnais region during four weeks of 2022 in order to image crustal structures and characterize active faults. We automatically detected and picked P and S waves with PhaseNet, resulting in a catalog of over 500 events, half of which are located beneath the temporary deployment. Tomographic images obtained from the inversion of P and S arrival times provide detailed insight into the geometry of folds and thrusts in the sedimentary cover, as well as the presence of a main fault in the basement which dips northward with an angle of 65° (Chaînons Béarnais normal fault). Seismicity relocation within the 3D model obtained by tomography shows that earthquakes are concentrated along this main active fault, extending from the top of the basement to a depth of approximately 16 km. These results demonstrate that passive imaging approaches can offer cost-effective alternatives to traditional controlled source imaging for seismotectonic studies and natural resource exploration in regions with active seismicity.

1. Introduction

The origin and distribution of intraplate earthquakes remain poorly understood. However, as pointed out by Sykes (1978), intraplate earthquakes tend to be concentrated along preexisting zones of weakness. A global compilation of earthquakes occurring within continental interiors revealed that intraplate seismicity is correlated with ancient rift systems (Schulte and Mooney, 2005). The Pyrenees are located within the Eurasia intraplate domain, far from the active plate boundary, which is located to the south of the Iberian peninsula. In the western Pyrenees, this seismicity is concentrated along a linear pattern that closely follows the southern boundary of the North Pyrenean Zone (Fig. 1). The moment tensor solutions for recent significant earthquakes in the Pyrenean domain have evidenced a predominant regime of extension normal to the orogen (Chevrot et al., 2011). This result is in good agreement with recent GPS studies which indicate a N-S extension rate across the Pyrenees of about 0.1–0.4 mm/yr (Rigo et al., 2015; Masson et al., 2019; Mazzotti et al., 2020), with no significant uplift in the Axial Zone (Masson et al., 2019), in contrast with the western Alps where it can reach up to 2.5 mm/yr (Nocquet et al., 2016). However, the

* Corresponding author.
E-mail address: sebastien.chevrot@get.omp.eu (S. Chevrot).

https://doi.org/10.1016/j.tecto.2024.230531
Received 4 April 2024; Received in revised form 9 October 2024; Accepted 10 October 2024
Available online 18 October 2024

processes driving this N-S extension and the present-day seismicity in the Pyrenees remain largely elusive.

In the Mauléon Basin, a recent seismotectonic study combined with local earthquake tomography has shown that the seismicity is located on the Lakora Fault, a major thrust fault that is now reactivated as a normal fault (Lescoutre et al., submitted). These results suggest that tectonic inheritance is indeed a key factor controlling the localization of deformation on major zones of crustal weakness. In this study, we focus on the Chaînons Béarnais region, which corresponds to the eastern limit of the Mauléon basin. This region is continuously active, in contrast to conventional seismic cycle models. It is characterized by the highest and most regular seismicity rate in the Pyrenees, as well as a lack of significant magnitude events (Sylvander et al., 2021). In fact, no earthquake has exceeded local magnitude 4.1 over the last thirty years. Interestingly, the $M_L = 5.5$ Arette earthquake of 1967, the last fatal earthquake to hit French territory, occurred on the western edge and outside this spot of enhanced activity.

In order to identify the main active faults in that area and their relationships to the geology, we have deployed a very dense array of ~100 three-component stations equipped with Stryde autonomous seismic nodes, with a regular spacing of approximately 1 km over a 10 × 10 km square area, complemented by a N-S profile with 100 stations spaced ~100 m apart (Fig. 2). This new generation of compact and low-cost autonomous nodes (Dieulangard et al., 2022) could potentially pave the way for local and regional deployments of thousands of sensors, a number that dwarfs conventional regional broadband deployments by several orders of magnitude. This experiment therefore provides an excellent opportunity to evaluate the potential of these low-cost nodes in a foothill environment for seismicity and passive imaging studies.

The paper is organized as follows. In section 1, we briefly describe the geological context of our study region, summarizing the recent geological knowledge of the Cretaceous rift system which was inverted during the Pyrenean orogeny. In section 2, we present the Arette passive acquisition which involved 600 one-component autonomous seismic nodes, recombined to get 200 three-component sensors. These nodes recorded ground acceleration for 28 days, from May 21 to June 18, 2022. Section 3 describes the workflow based upon PhaseNet (Zhu and Beroza, 2019), a deep convolutional neural network that automatically detects and picks P and S phases from local earthquakes. During the experiment, we were able to detect and locate 550 events. The resulting catalog was then used to perform a local earthquake tomography with PStomo (Tryggvason et al., 2002). The tomographic method and the resulting model are described in section 4. Finally, we present geological interpretations of our tomographic images, and discuss the relationships between seismicity and the active faults imaged with tomography.

2. Geological and tectonic contexts

The Pyrenean belt is the result of the convergence of the Iberian and Eurasian plates during the Santonian to Oligocene (Puigdefàbregas and Souquet, 1986; Olivet, 1996; Angrand et al., 2020). Continental collision led to the formation of a double-vergent *E*-W orogenic belt characterized by different structural domains: from south to north, the south-Pyrenean Zone, the Axial Zone, the north-Pyrenean Zone and the Aquitain foreland basin (Choukroune, 1976). The Axial Zone corresponds to imbricated Paleozoic units that overlap the South Pyrenean Zone while the North Pyrenean Zone comprises a system of inverted Mesozoic rift basins overlapping the Aquitaine foreland basin (Mouthereau et al., 2014; Teixell et al., 2016; Espurt et al., 2019). In the study area (Fig. 1), located in the western Pyrenees, the North Pyrenean Zone is represented by the inverted Mauléon basin. This basin developed in the Lower Cretaceous in response to hyperextension of the continental crust that lead to mantle exhumation (Jammes et al., 2009; Lagabrielle et al., 2010, 2020; Masini et al., 2014; Saspiturry et al., 2019; Lescoutre et al., 2019; Lescoutre and Manatschal, 2020). The basin formation was controlled by the concomitant development of a N120° longitudinal detachment system (Masini et al., 2014; Saspiturry et al., 2021) and N20° transverse faults (Canérot, 2017), the most important of which is

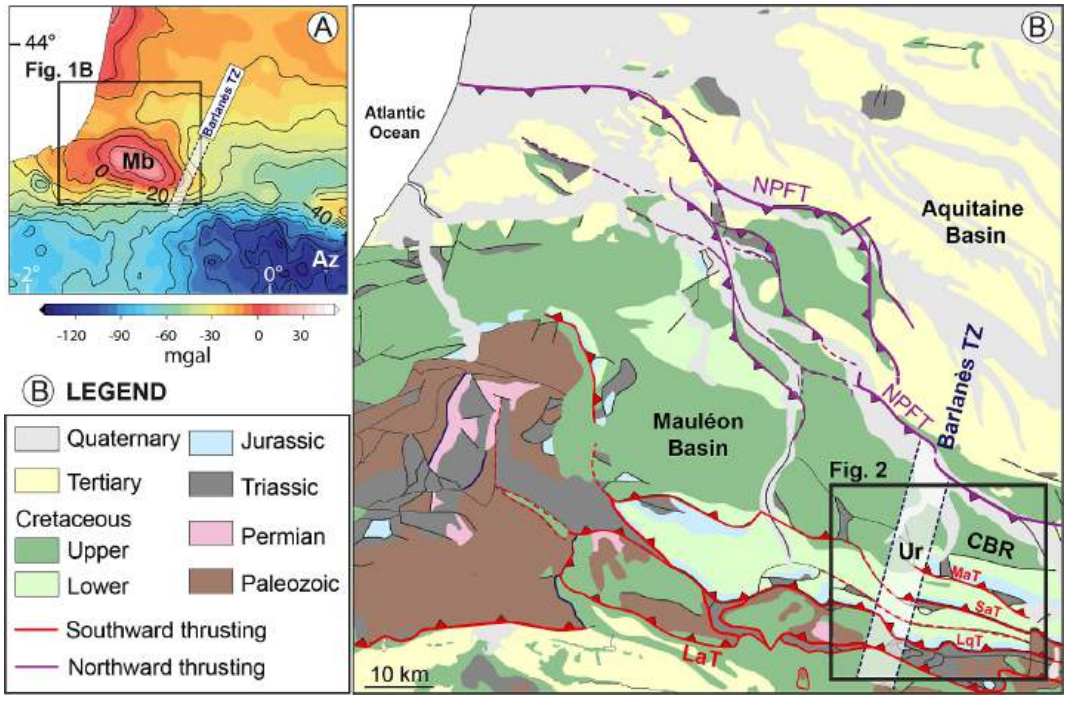

Fig. 1. (A) Map of Bouguer gravity anomalies in the Western Pyrenees showing a negative anomaly in the Axial Zone (AZ) and a positive anomaly in the Mauléon basin (Mb), which is delimited by the Barlanès Transfer Zone to the east. (B) Structural map of the Mauléon basin with its flanking thrust faults (Location shown in Fig. 1A). Main north-vergent and south-vergent thrust faults are shown in purple and red, respectively. Ur: Urdach lherzolites; CBR: Chaînons Béarnais Range; NPFT: North Pyrenean Frontal Thrust; LaT: Lakora Thrust; MaT: Mail Arrouy Thrust; SaT: Sarrance Thrust; LqT: Licq Thrust; TZ: Tranfer Zone. (For interpretation of the references to colour in this figure legend, the reader is referred to the web version of this article.)

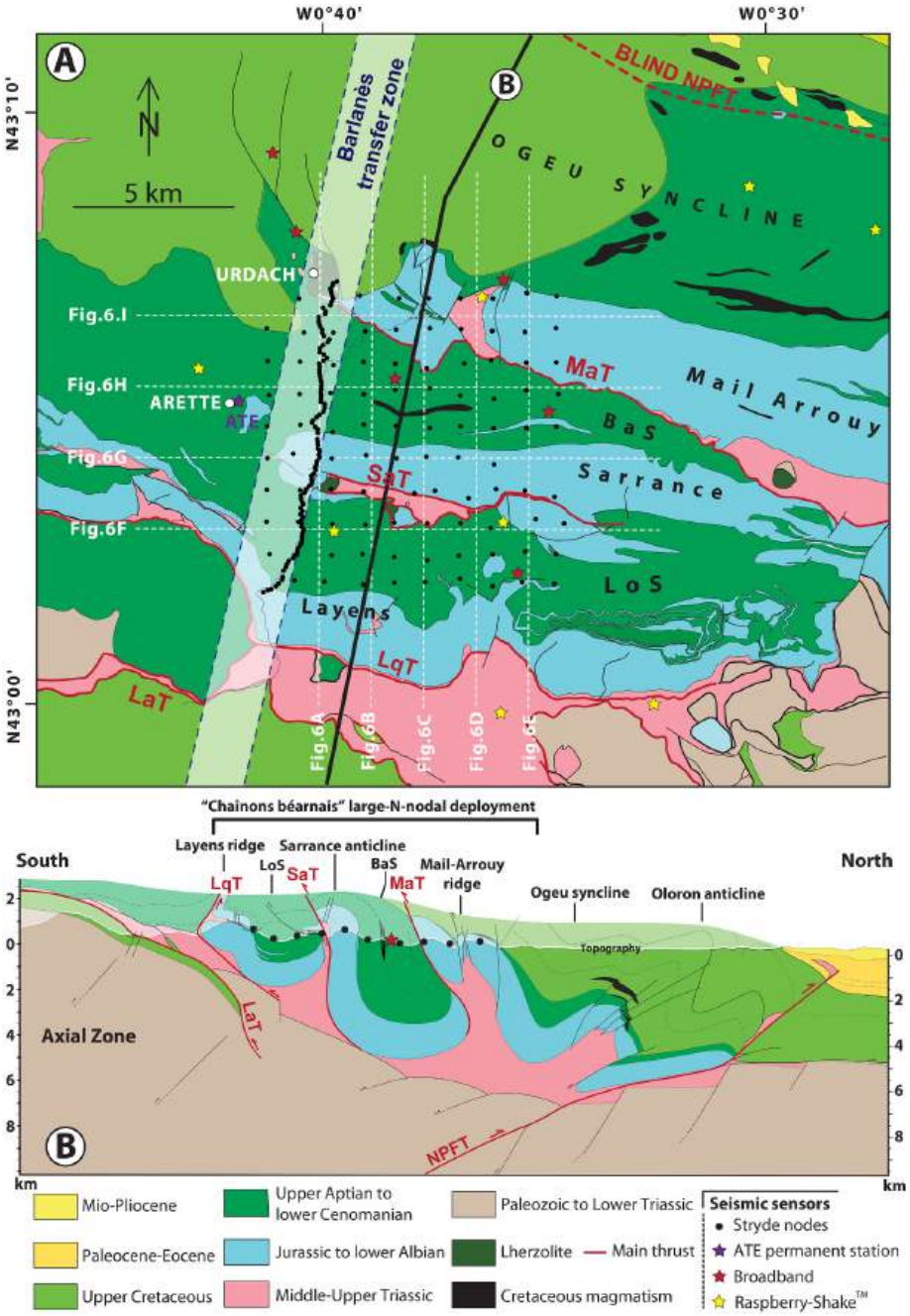

Fig. 2. (A) Geological map and (B) geological cross-section of the study area from Labaume and Teixell (2020). From south to north: Ogeu syncline, Mail Arrouy ridge, Barescou syncline (Bas), Sarrance ridge, Lourdios syncline (LoS), and Layens ridge. NPFT: North Pyrenean Frontal Thrust; MaT: Mail Arrouy Thrust; SaT: Sarrance Thrust; LqT: Licq Thrust; LaT: Lakora Thrust. The Stryde sensors are shown with black circles, and the Broadband stations (Güralp CMG40-T sensors) with red stars. The permanent broadband station Arette (ATE) of the French national network is shown with a purple star. (For interpretation of the references to colour in this figure legend, the reader is referred to the web version of this article.)

the N20° Barlanès lithospheric Transfer Zone (BTZ) (Fig. 1) (Saspiturry et al., 2022, 2024). The relics of this rifting phase are still visible today. Indeed, the western part of the Mauléon basin coincides with the large positive Labourd Bouguer gravity anomaly, which is bounded to the east by the BTZ (Fig. 1). Recent passive imaging studies (Wang et al., 2016; Lehujeur and Chevrot, 2020; Chevrot et al., 2022) and joint gravimetric and magnetic 2D forward modeling (Saspiturry et al., 2024) have linked this anomaly to the presence of exhumed subcontinental mantle preserved in the former hyperextended rift domain. Thus, the BTZ represents a *syn*-collisional lithospheric transfer zone delimiting a western domain where the mantle is preserved at shallow depth from an eastern domain where the Pyrenean compression succeeded in bringing the mantle back to depth and thickened the continental crust (Lehujeur and Chevrot, 2020; Saspiturry et al., 2024).

The orogenic segment of the Chaînons Béarnais, the eastern counterpart of the Mauléon basin, is characterized by a succession of south-verging thrusts and folds oriented N120° (Fig. 2). In this part of the belt, the Axial Zone is separated from the North Pyrenean Zone by the south-verging Lakora thrust (Teixell, 1998; Teixell et al., 2016). To the north, the Chaînons Béarnais are separated from the Axial Zone by the Bedous Triassic unit delimited to the north by the sub-vertical Licq fault (Fig. 2) (Labaume and Teixell, 2020). The Chaînons Béarnais consist of a system of Jurassic to Lower Cretaceous carbonate antiformal/thrust ridges of diapiric origin (Mail Arrouy, Sarrance and Layens ridges), which are

separated by thick *syn*-rift salt-controlled mini-basins (Ogeu, Barescou and Lourdios synclines) (Fig. 2) (Canérot, 1988; James and Canérot, 1999; Canérot et al., 2005; Labaume and Teixell, 2020). Shortening of this sedimentary cover during the proto-collisionnal stage caused folding and diapir squeezing (Labaume and Teixell, 2020). To the north, the Chaînons Béarnais straddle the Aquitaine foreland basin along the North-Pyrenean Frontal Thrust (Angrand et al., 2018; Issautier et al., 2020, 2022; Ortiz et al., 2020, 2022). In the study area, the North-Pyrenean Frontal Thrust is blind and marked at the surface by the Oloron anticline (Fig. 2) (Labaume and Teixell, 2020).

The Chaînons Béarnais area has an unusual seismicity, characterized by its continuous and regular occurence. Fig. 3 shows earthquake locations extracted from the Observatoire Midi Pyrénées catalog (Sylvander et al., 2021). Due to significant location uncertainties and the lack of surface fault traces (Lacan and Ortuño, 2012), the identification of active faults associated with this seismicity remains uncertain. Previous studies (e.g., Rigo et al., 2005) have concluded that the seismicity is not correlated with a hypothetical North Pyrenean Fault that would mark the boundary between the Axial Zone and the North Pyrenean Zone. Instead it would be associated with other poorly constrained crustal structures affecting the North Pyrenean Zone. For these reasons, all faults depicted on the geological map (Fig. 2) are generally

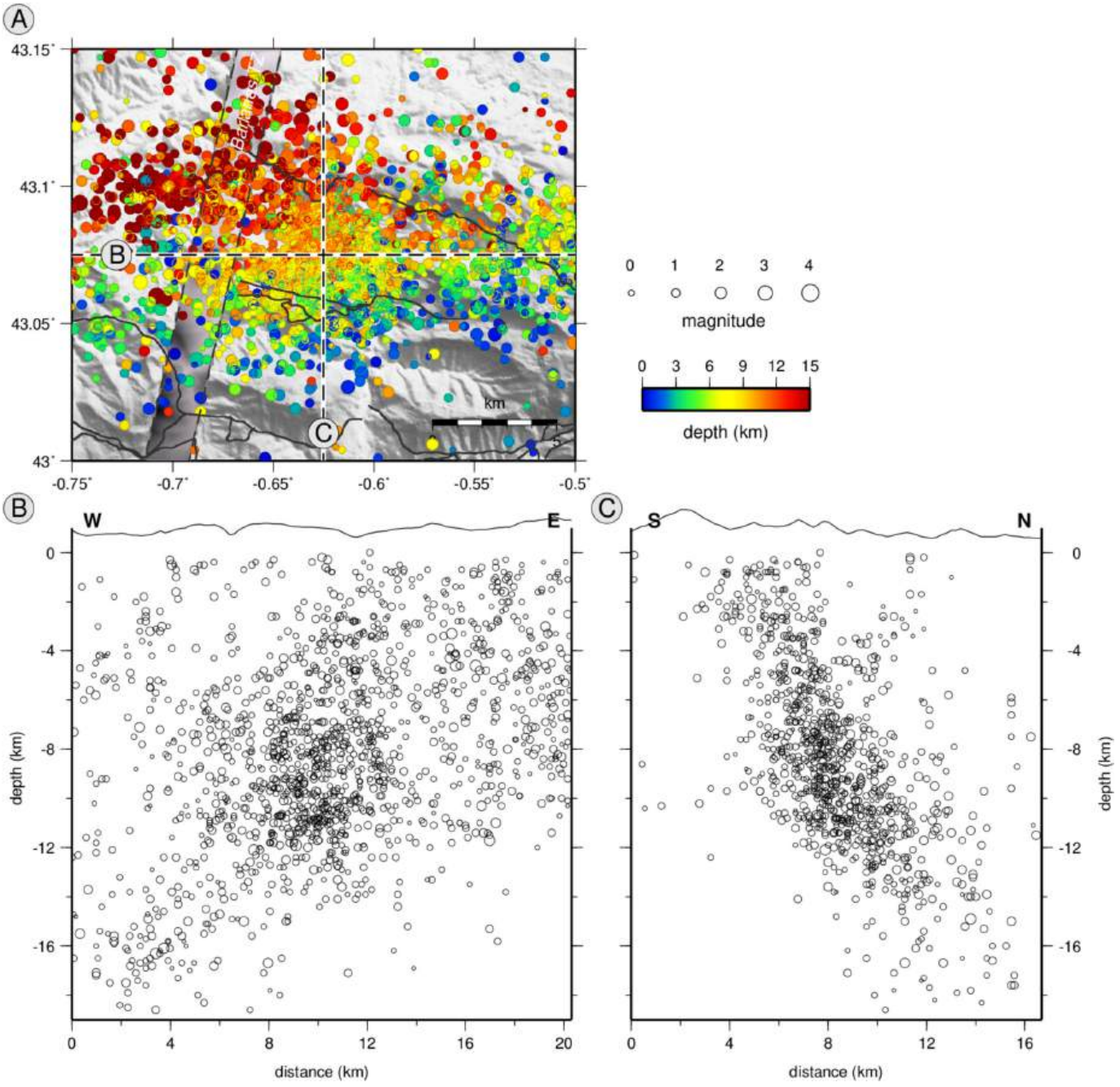

Fig. 3. Long-term seismicity in the Chaînons Béarnais region recorded by permanent networks. Events are from the catalog of Sylvander et al. (2021) encompassing the 1989–2019 period and updated to 2021. Only hypocenters of quality "A" on a 4-grade scale are represented, i.e. 2032 events. The estimated horizontal and vertical uncertainties are of the order of 2 km. (A) Map view, with event size proportional to magnitude, and colour related to focal depth. Dashed lines correspond to the positions of the cross-sections. (B) S/N cross-section. (C) E/W cross-section. In both cross-sections, the scale is the same for distance and depth, and the projection width is ±3 km.

considered as potentially active (Rigo et al., 2005; Dubos-Sallée et al., 2007; Lacan and Ortuño, 2012). However, they are not all of equal importance and therefore should not represent the same seismic risk. Indeed, some of them are considered as significant thick-skin structures such as the BTZ deeply rooted in the upper lithosphere (Saspiturry et al., 2024) and the Lakora thrust and the North-Pyrenean Frontal thrust which affect the basement (Teixell, 1998; Teixell et al., 2016; Labaume and Teixell, 2020). On the other hand, the Licq, Sarrance and Mail-Arrouy structures are considered more superficial and only affect the sedimentary cover (Fig. 2) (Labaume and Teixell, 2020). Therefore, identifying which of these structures are active and comprehending their geometry remains crucial for assessing seismic hazard in this region, which is regularly hit by moderate-sized earthquakes.

3. The Arette acquisition

The Arette experiment involves a new type of sensor coming from the field of active seismic, and hitherto little used in seismology. These are single-component autonomous nodes from the Stryde company (Ourabah et al., 2021). Each node weighs 150 g and has a cylindrical dimension of 13 × 4 cm (Fig. 4A), making it easy to transport and deploy hundreds of them in difficult-to-access terrains such as the Pyrenees. Each node is equipped with a GNSS system for synchronization and positioning, and has a sealed waterproof container with no connector point, which is useful for withstanding harsh weather conditions. The sensor inside the node is a piezo-electric accelerometer with a flat response between 1 and 125 Hz, although frequencies from 0.5 to ~200 Hz are captured. These nodes can also be used to record shear waves if installed horizontally (Ourabah et al., 2021). We took advantage of this specification and combined three of these nodes at each measurement site to emulate a three-component sensor. The two "horizontal" sensors were coupled at 90° by a metal support. The vertical sensor was left free so that it could be moved a few centimeters around the horizontal support during the planting process, depending on the requirements of the terrain (Fig. 4B). The nodes were activated at the time of deployment but put into sleep mode. Using the calendar function available with this system, the recording was programmed to start after the expected last deployment day so that the entire network would start recording on the same date.

The acquisition (Fig. 2 combines two different deployments, each comprising around ~100 stations. The first deployment consists of a regular rectangular grid, with an inter-station distance of around 1 km. The second deployment is a more or less linear south-north transect, mainly along low-traffic roads, with a spacing of 100 m. The topography of the terrain presented a first challenge. Indeed, the study area is characterized by a rugged relief, composed of several anticlinal and synclinal folds roughly oriented east-west, intersected by two valleys oriented north-south (to the west the Lourdios valley and to the east the Aspe valley). Altitudes range from 200 m to 1500 m. The positioning of the 2D grid is the result of a compromise to take account of this topography and maintain a regular grid geometry. It was not possible to find a configuration that would allow all the nodes to be installed, and two locations had to be abandoned because their theoretical locations, on a steep ridge, were inaccessible under reasonable safety conditions. The point located in the north-western corner of the grid was also not installed, as access to it would have required disproportionate travel time compared to the marginal interest of this location for tomography. Actual field conditions meant that the final positions of the stations varied by a few dozen meters from the initial regular grid (62 m on average, maximum deviation 235 m, 82 % of points less than 100 m from their theoretical location). This regularity was one of the experiment's prerequisites, as it guarantees greater efficiency in detecting and locating earthquakes, as well as in local earthquake tomography.

For the transect, the sinuosity of the roads also had to be taken into account. For faster deployment, it was decided, unlike the 2D grid, to stay along existing roads without deviating from them by more than a few meters. The transect was designed by projecting points spaced 100 m apart on a straight line oriented N13 (according to the azimuth of the main road). The regularity of the deployment can be measured by the distance between two successive stations. The average of these distances is 128 ± 60 m. Fig. 2 shows the profile finally obtained, which roughly follows this N13 azimuth. The soils in which the instruments were installed were fairly homogeneous, with almost everywhere on the 2D grid a layer of soil sufficient to plant the vertical sensor by a few centimeters, and cover the horizontal sensors with a thin layer of soil. Moisture conditions, on the other hand, were highly variable: while

Fig. 4. The Stryde autonomous nodes used in the Arette acquisition (a). At each site we deployed three mono-component units to simulate a three component sensor (b).

most soils were relatively dry, they could be very wet in the woods, occasionally affecting the GNSS performance of the nodes. Along the transect, a large proportion of the nodes were placed in road embankments, made up of unconsolidated and dry gravel. Deployment was completed in seven working days, in four shifts. Some points on the grid required several hours' walking, while the entire profile was installed in a single day. The device recorded for 28 days, from May 21 to June 18, 2022, at 500 samples per second. The data were converted from SEG-rev3 to miniseed format, and resampled at 100 samples per second. The final total volume of useful data is 413 Gb.

A combination of very wet soil and deeper depth of burial of the vertical component (compared to the horizontal ones) posed challenges for GNSS synchronization on the vertical component for some of the stations. This could be avoided if the survey was repeated, based on lessons learned in the project. Nevertheless, data recovery was good for the vertical channels (59 % for the grid, 70 % for the profile) and very good for the horizontal channels (96.7 % for the grid, 97.4 % for the profile), which performed much better due to their shallower burial depth. Due to the loss of vertical components, which makes P-wave picking more difficult, we modified the automatic picking procedure performed with PhaseNet (Zhu and Beroza, 2019), as described below. In addition to the Stryde nodes, we were also able to benefit from the presence of permanent and temporary stations already in place in the study area. The permanent stations belong either to the French RESIF-EPOS permanent network (https://www.epos-france.fr/en), in which case they are mainly equipped with broadband sensors and marginally with accelerometric sensors, or to the RaspberryShake™ network deployed by the Université de Pau et des Pays de l'Adour (UPPA) in the central and western Pyrenees. In addition, a temporary mini-array of 6 stations (CMG40-T sensors) had been in place for two years at the time of deployment. Data collected by these sensors during the Arette experiment have been added to the dataset.

4. Automatic phase picking, phase association and preliminary event location

Thanks to the density of our deployment, we can accurately detect and locate events of very small magnitude (down to −1, and in favorable cases, even lower), thus lowering the magnitude threshold by several units compared with the catalog derived from the permanent seismic network. Therefore, we have access to a much finer and more complete characterization of the seismicity and active faults, and to a potentially large catalog of P and S picks that can be exploited to obtain finely resolved images of crustal structures with local earthquake tomography.

For the purpose of this study, and to process the large amount of data generated by our temporary instrumentation (~1.4×10^9 s of recordings), we used PhaseNet (Zhu and Beroza, 2019), a deep neural network picker that automatically detects and picks regional Pg/Sg phases. Trained on a large dataset of nearly 800.000 three-component records of Californian earthquakes, PhaseNet has already demonstrated its ability and efficiency to detect and pick local and regional phase arrivals in different tectonic settings (Retailleau et al., 2022; Ammirati et al., 2022; García et al., 2022; Derode et al., 2023). By calculating the time differences between manual picks made by seismic analysts and PhaseNet automatic picks, these authors documented arrival time pick variations of less than 0.15 s, which is comparable to what is observed when comparing two different human analysts. In our study, in order to test the sensitivity of our instrumentation and ensure that as many seismic events as possible are recorded, we used a low 0.3 probability threshold in the PhaseNet algorithm for both P and S phases. We performed an initial analysis of the complete dataset (6 temporary stations ARE, permanent broadband station ATE, 15 Raspberryshake, and 200 three-component nodes) with PhaseNet, retaining only those stations for which all three components were available (80 % of the stations from the linear profile, and 66 % from the regular 2D grid). We then associated the 2.489.495 resulting P and S picks with REAL (Zhang et al., 2019). The REAL algorithm associates the P and S picks that potentially belong to the same seismic event, using travel times computed in the 1D Pyrenean velocity model of Pauchet et al. (1999). It provides a rapid preliminary location and a subsequent refined location by identifying optimal minima of residual times using the simulated annealing method. To reduce the number of false detections due to the low PhaseNet threshold of 0.3, we set the number of minimum P and S arrivals for event detection to 10 and 5, respectively. After processing the ~2.5 Mpicks previously identified, 52,995 were kept after association, resulting in the detection of 590 events. Using these preliminary hypocentral locations, we then rotated the horizontal components of stations for which the vertical component was missing to obtain the radial and transverse components. We then performed a second data analysis with PhaseNet, using the radial component in place of the vertical component where it was missing. This procedure provided 17.000 new picks, i.e. 32 % of the original number of picks. We relocated all the events with NonLinLoc (Lomax et al., 2000) in the 1D model, using the updated catalog which contain 33,124 P and 36,311 S picks. We end up with a reliable catalog of 556 events displaying a mean residual of 0.05 s and a mean location uncertainty of 0.35 km. Fig. 5 shows examples of automatic PhaseNet picks.

Magnitudes (M_L type) were calculated, for each event, by averaging the maximum amplitude over the three-component displacement signals (native or reconstructed) for the stations that recorded that particular event. Although the absolute response of the Stryde nodes is known in acceleration, it was possible to calibrate them by collocating certain nodes with velocimetric stations with known response (permanent or semi-permanent stations equipped with conventional hardware). The attenuation law used is the one conventionally adopted for the Pyrenees (Sylvander et al., 2021), which recalibrates the magnitudes to the most stable scale in mainland France, that of the LDG-CEA (Duverger et al., 2021).

5. Results

5.1. Local earthquake tomography

We performed local earthquake tomography (LET) to image crustal structures beneath the temporary deployment, following the same methodology as in our previous studies (see Lehujeur and Chevrot, 2020; Chevrot et al., 2022; Lescoutre et al., submitted). From the catalog, we selected events with at least 8 P picks and 4 S picks, with an azimuthal gap smaller than 200°. Given the density of the array, this ensures that all selected events are located with sufficient accuracy for tomography. For inversion, we only select source-station paths for which we have both P and S picks. The idea is to attenuate the differences in the V_P and V_S models that might result from a difference in ray coverage. Applying these selection criteria, the dataset comprises 209 earthquakes and 14,673 P and S picks. On average, for each event, we have more than 70 recording stations.

For the tomographic inversion, we use the code PStomo, based on Benz et al. (1996), and modified by Tryggvason et al. (2002) to simultaneously invert P and S travel times. Travel time tables in the 3-D models are calculated using the finite-difference code of Podvin and Lecomte (1991) in the inversion grid, which has dimensions of 20x20x25 km. The tomographic method iteratively inverts the 3-D V_P and V_S models and the earthquake locations, as advocated by Thurber (1992). The P and S travel time tables are recalculated at the start of each iteration for the current 3-D V_P and V_S models. The V_P and V_S models are parameterized with homogeneous 600 m cubic blocks. We perform different inversions, shifting these blocks by 0, 200, and 400 m along the three dimensions, and calculate the mean V_P and V_S models from these 27 different inversions. After averaging the 27 offset models, we obtain V_P and V_S models with a discretization of 200 m. The starting model used in the inversion is the 1-D velocity model used for earthquake location (Pauchet et al., 1999). The final 3D model was obtained

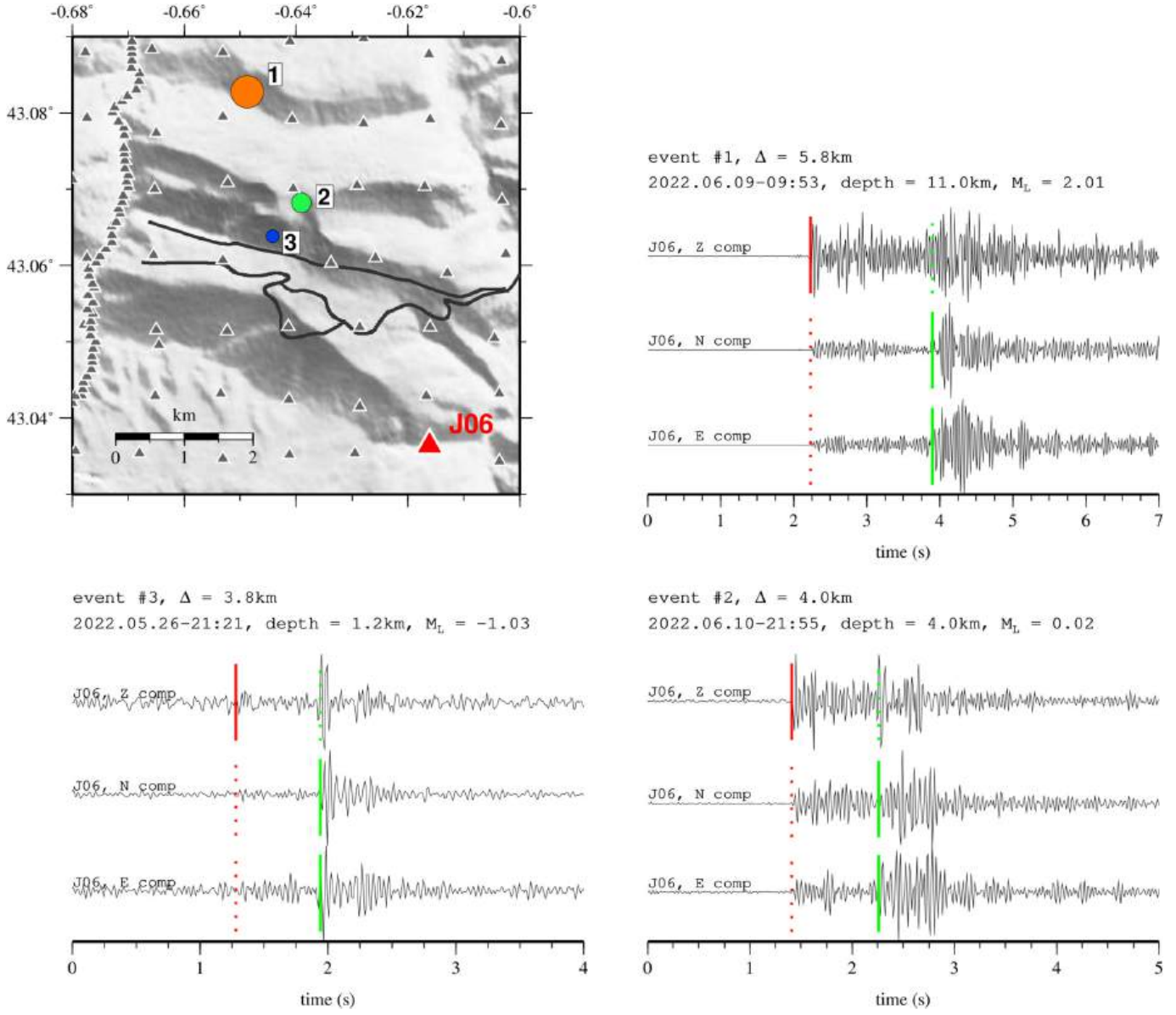

Fig. 5. Examples of automatic P and S picks performed with PhaseNet on station J06. The 3 chosen events are plotted on the map in the upper left panel, (colored circles), together with the recording station (red triangle); they cover a wide range of magnitudes (from −1 to 2) and depths (from 1 to 12 km). In red (resp. green) the P (resp. S) PhaseNet picks. (For interpretation of the references to colour in this figure legend, the reader is referred to the web version of this article.)

after 10 iterations. The initial root-mean square (RMS) error of arrival times was 0.116 s for P waves and 0.098 s for S waves, and the final RMS was 0.076 s for P waves and 0.047 s for S waves. This represents a 57 % reduction of variance for P-waves, and 77 % for S-waves. These numbers suggest that the quality of the S picks is superior to that of the P picks. This intriguing observation can be explained by the fact that we are using accelerometers, which have a lower sensitivity compared to classical velocimetric geophone nodes. Since we are exploiting very small earthquakes, with magnitude below 0 for most of them, the less energetic P arrivals may be less easily detected and picked by PhaseNet than S waves.

The domain in which structures are well resolved is primarily controlled by the distribution of seismicity. Since the deeper events are found at about 20 km depth within a narrow north-dipping active fault system, ray coverage is limited tp the upper 10–15 km of the crust. We have performed checkerboard resolution tests which show that we have a good spatial resolution down to at least 10 km depth (Figs. S1-S4). Fig. 6 displays several N-S cross-sections in the final V_P model. A similar Figure showing the V_S model can be found in the supplementary material (Fig. S5). At first order, the velocity model shows two domains with contrasting velocities, approximately separated by the isovelocity 5.4 km/s for P waves (and 3.3 km/s for S waves). Low seismic velocities, below 5.4 km/s, are observed above this interface, which corresponds to the structural detachment level of the Chaînons Béarnais folds, known as the Upper Triassic salt unit, thus materializing the basement/sedimentary cover interface. The depth and geometry of this decollement are consistent with previously published crustal-balanced cross-sections of the Chaînons Béarnais (Dubos-Sallée et al., 2007; Teixell et al., 2016; Labaume and Teixell, 2020). Therefore, the thickness of the Chaînons Béarnais sedimentary cover ranges from 2 km in the south, to up to 3.5 km in the north. It corresponds to salt-controlled sedimentation in the former hyperextended rift domain of the early Cretaceous eastern Mauléon basin, now shortened and preserved in a pop-up (Labaume and Teixell, 2020). Isovelocity lines for V_P below 5.4 km/s are folded and correspond fairly well to fold structures of the Chaînons Béarnais recognized on the surface. Large synclines are represented by velocity

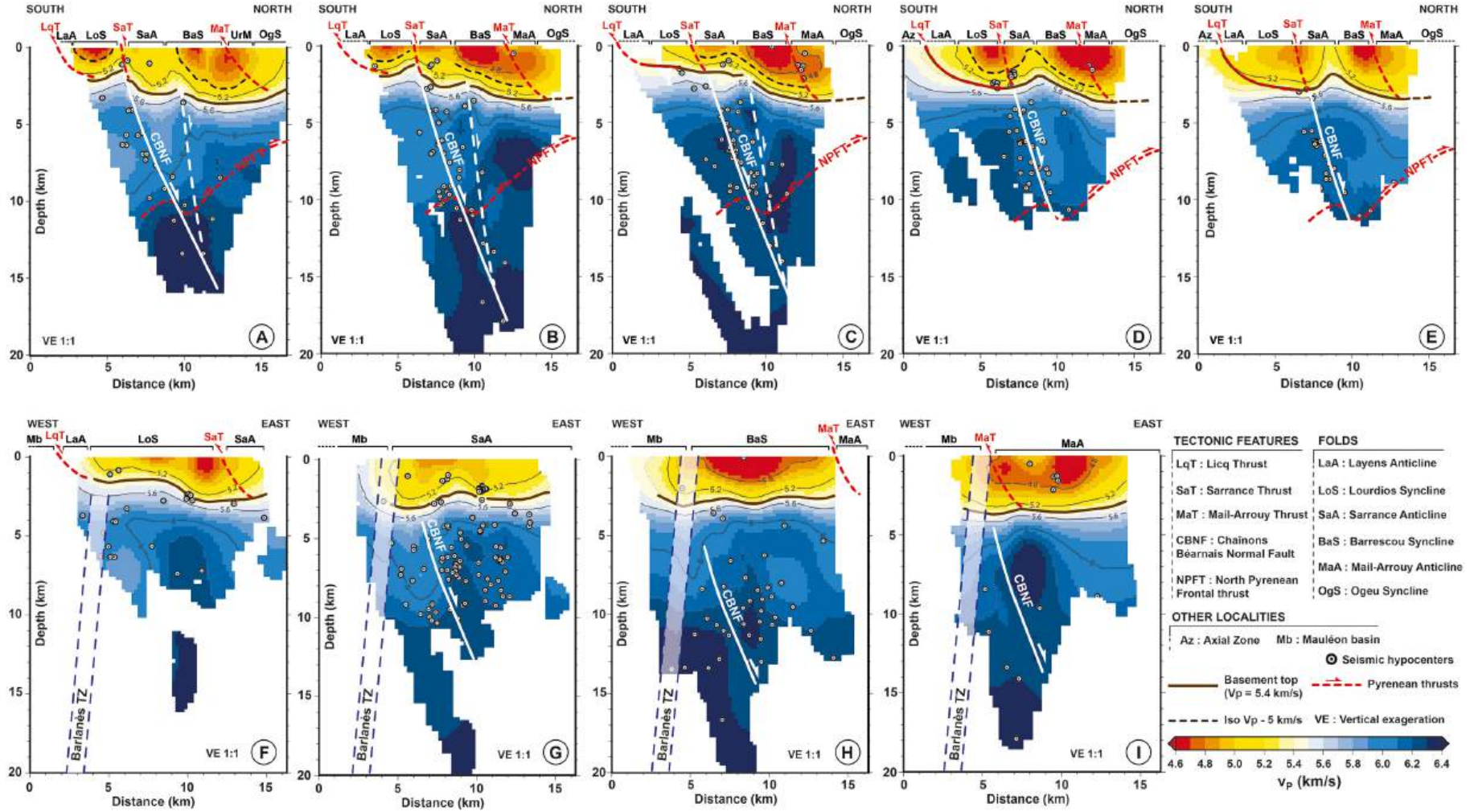

Fig. 6. Interpreted local earthquake tomography V_P model. (A-E) North-South sections; (F—I) West-East sections. See Fig. 2 for section location.

values below 4.8 km/s (Lourdios (LoS) and Barescou (BaS) synclines on Fig. 6), while tight anticlines are associated with V_P between 4.8 and 5.2 km/s (Sarrance (SaA) and Mail Arrouy (MaA) anticlines on Fig. 6). These velocities are consistent with the nature of the sedimentary rocks, which correspond to Jurassic to Lower Cretaceous platform carbonates in the anticlines and thick Cretaceous flysch in the synclines. The south-verging thrusts bordering the Layens, Sarrance and Mail-Arrouy anticlines are rooted at depth on the basement/sedimentary cover interface (isovelocity 5.4 km/s for P waves), as the latter does not appear to be displaced by these structures.

Beneath the sedimentary cover, we document compressional velocities ranging from 5.4 to 6.4 km/s. These seismic velocities are characteristic of Hercynian basement rocks. On the north-south cross-sections, we identify several north-dipping structures that separate blocks with different seismic velocities. Among these, a fault, referred to hereafter as the Chaînons Béarnais Normal Fault (CBNF), shows a particularly clear and strong signature in the velocity model, which can be followed laterally along the different sections. The CBNF plunges steeply northwards at an angle of around 65°. It is interpreted to affect at depth the former North Pyrenean Frontal Thrust although the velocity model does not allow us to precisely constrain the geometry of this north-verging thrust. The CBNF seems to be reactivating the Sarrance thrust, as suggested by the apparent offset of the sediment/basement interface, which is particularly clear in the westernmost section (Fig. 6A). On the *E*-W cross-sections (Figs. 6F-I), we observe an almost vertical boundary (parallel dashed lines) located slightly east of the dense N-S transect, coinciding with the Barlanès Transfer Zone, and the signature of the CBNF, which is slightly oblique to these sections.

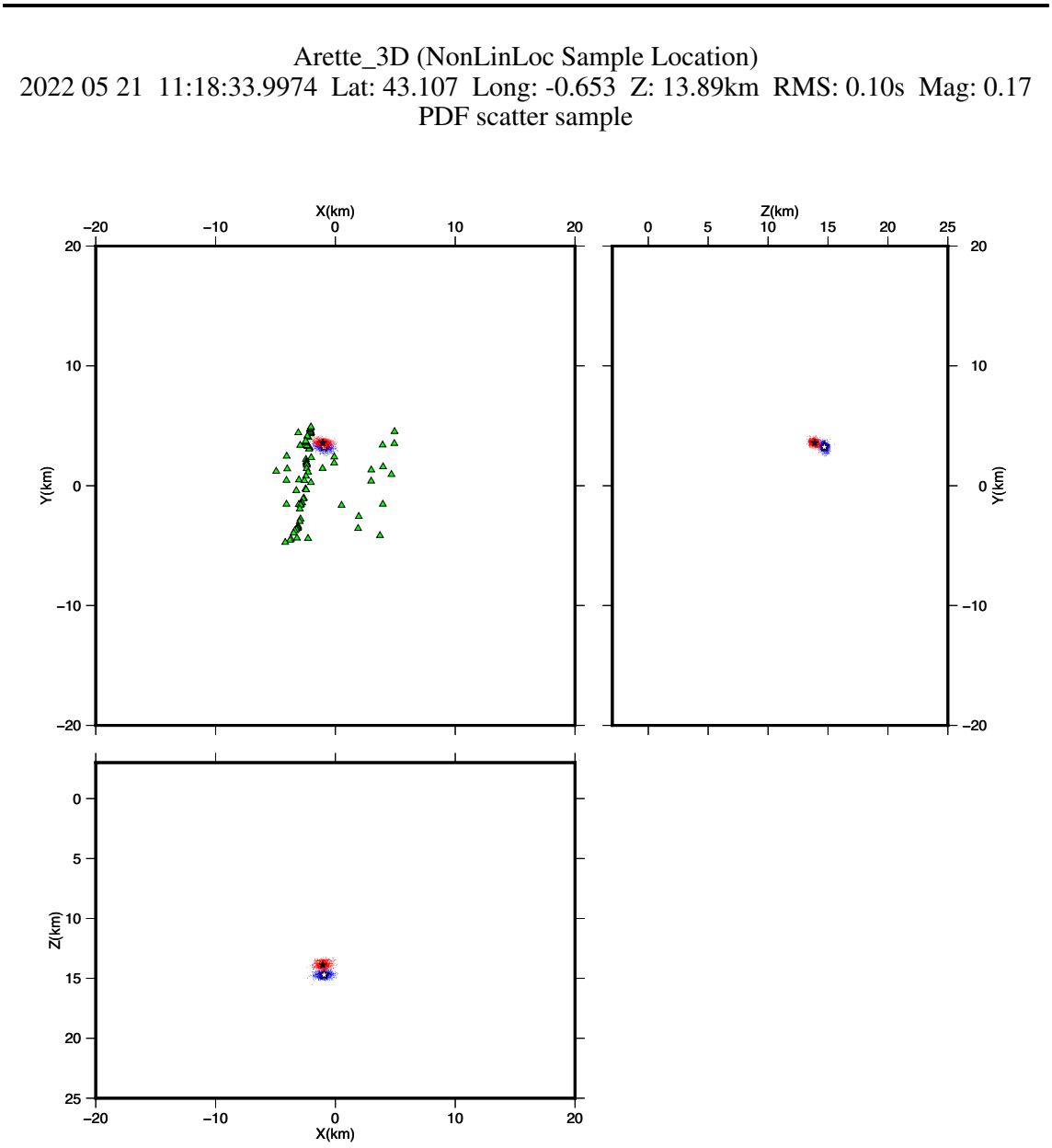

Fig. 7. Probability density function for the location of the magnitude 0.17 May 21, 2022 event. The blue and red dots show the 50,000 scatter samples drawn from the octree search for the locations in the 1D and 3D models, respectively. The green triangles show the stations that provided P and/or S picks. The 1D and 3D hypocenter locations have a vertical shift of 800 m, well above the ~200 m vertical confidence interval for both 1D and 3D locations. (For interpretation of the references to colour in this figure legend, the reader is referred to the web version of this article.)

5.2. Relocation of seismicity in the 3D model with NonLinLoc

The 3D V_P and V_S models obtained with local earthquake tomography have been used to relocate the complete catalog of seismicity with NonLinLoc (NLL) (Lomax et al., 2000), an importance sampling method that explores the entire space of source parameters (Tarantola and Valette, 1982). The main advantage of this approach is that it allows us to determine confidence regions for these source parameters and avoids the errors induced by linearization of the source location problem (Pavlis, 1986). We first create a 40 × 40 km grid centered on a reference point located at 43.075°N and − 0.64°W, going from 3 km above the sea level down to 20 km depth. The P and S velocity models are discretized with 0.2 km cubic blocks. The code first computes the P and S travel time grids in the 3D models for each station of the array with the finite-difference method of Podvin and Lecomte (1991). Using these pre-computed travel time tables, NonLinLoc then performs an oct-tree Monte Carlo search to sample the posterior density function (pdf) of source parameters (origin time and 3D hypocenter location).

Fig. 7 shows the 50,000 samples of the PDF obtained from the NLL oct-tree search for the magnitude 0.17 earthquake of May 21, 2022, in both 1D and 3D models. This event, located from the 77 P and 77 S picks obtained at the stations represented by the green triangles in Fig. 7, is representative of the population of earthquakes that were recorded during the experiment. The 1D (blue dots) and 3D (red dots) sampled

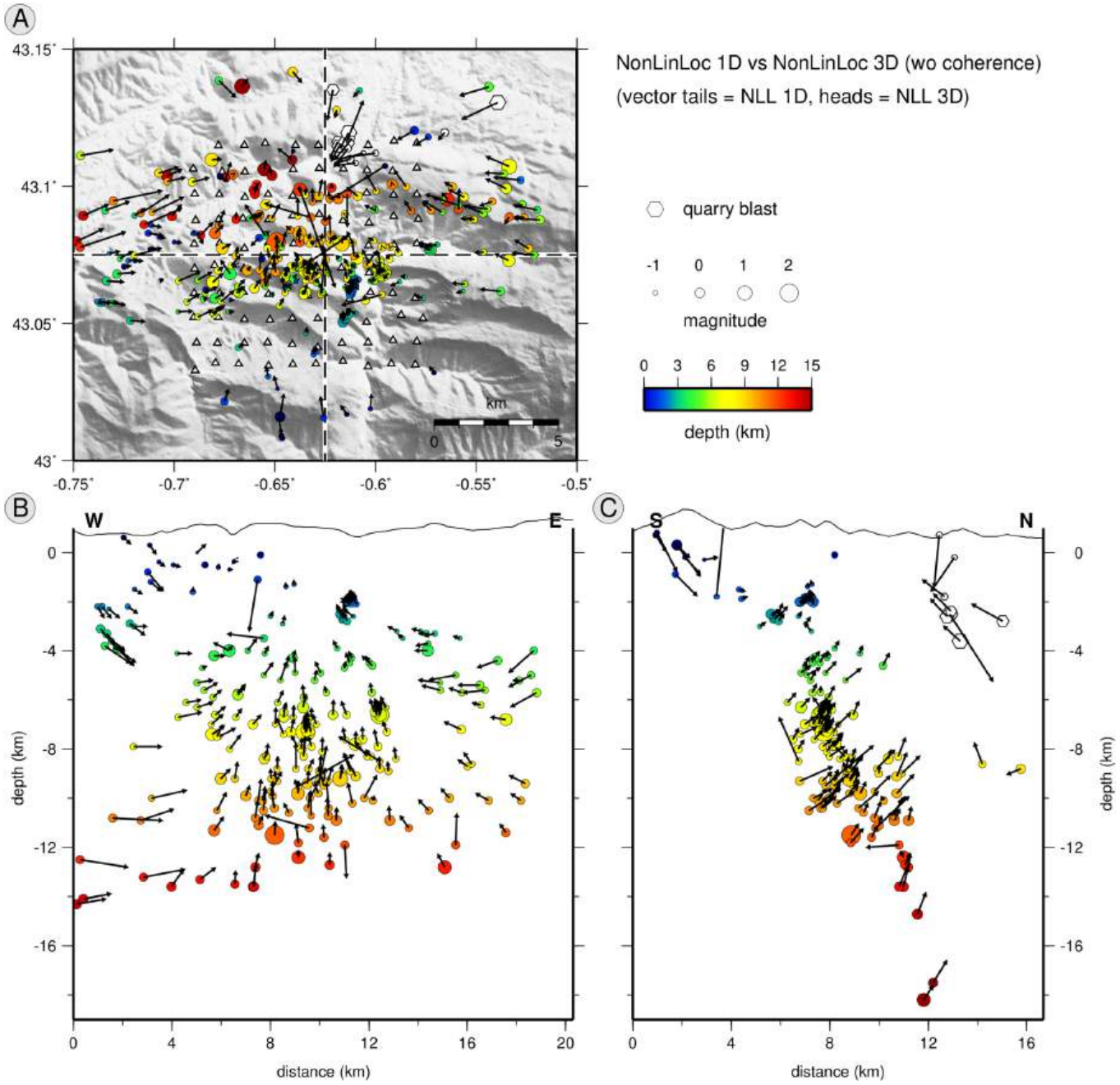

Fig. 8. Effect of the 3D model on earthquake locations. a) Map showing the epicenters (colored circles) located in the 1D model, stations (white triangles), and relocation vectors (black arrows), pointing from 1D to 3D locations. The size of the circles scales with the magnitude and the colour code indicate the depth of the events. White hexagons are identified quarry blasts. The dashed lines show the positions of the *E*-W and N-S cross-sections. b) E-W vertical cross-section showing the hypocenters and relocation vectors, projected on the vertical plane. c) same as b) but for the N-S vertical cross-section. In both cross-sections, the scale is the same for distance and depth, and the projection width is ±3 km.

pdfs show limited dispersion around the maximum likelihood solutions, materialized by white (1D) and black (3D) stars. The horizontal and vertical uncertainties, derived from the 68 % confidence interval, are around 600 m and 200 m, respectively. In our example, the 1D and 3D locations are relatively close, being separated by only about 800 m. However, the 3D hypocenter is clearly located beyond the 200 m vertical confidence interval of the 1D location. These simple observations suggest that statistical errors derived from probabilistic location methods should not be taken at face value. They merely reflect the uncertainties resulting from measurement errors made when P and S phases are picked on seismic records. The bias resulting from using inacurrate velocity models is usually much greater. Our results are in line with synthetic experiments which have shown that locations using 1D approximations of 3D models lead to systematically biased solutions and that the confidence region usually does not include the "true" location (Pavlis, 1986; Wittlinger et al., 1993; Lomax et al., 2000).

Fig. 8 shows the variations in hypocenter location resulting from using the 3D local earthquake tomography model described above. The relocation vectors, represented by black arrows pointing from 1D to 3D locations, show that events beneath the array are pulled towards the surface while events located outside the array tend to be drawn towards the center of the deployment. For outside events located more than 8 km

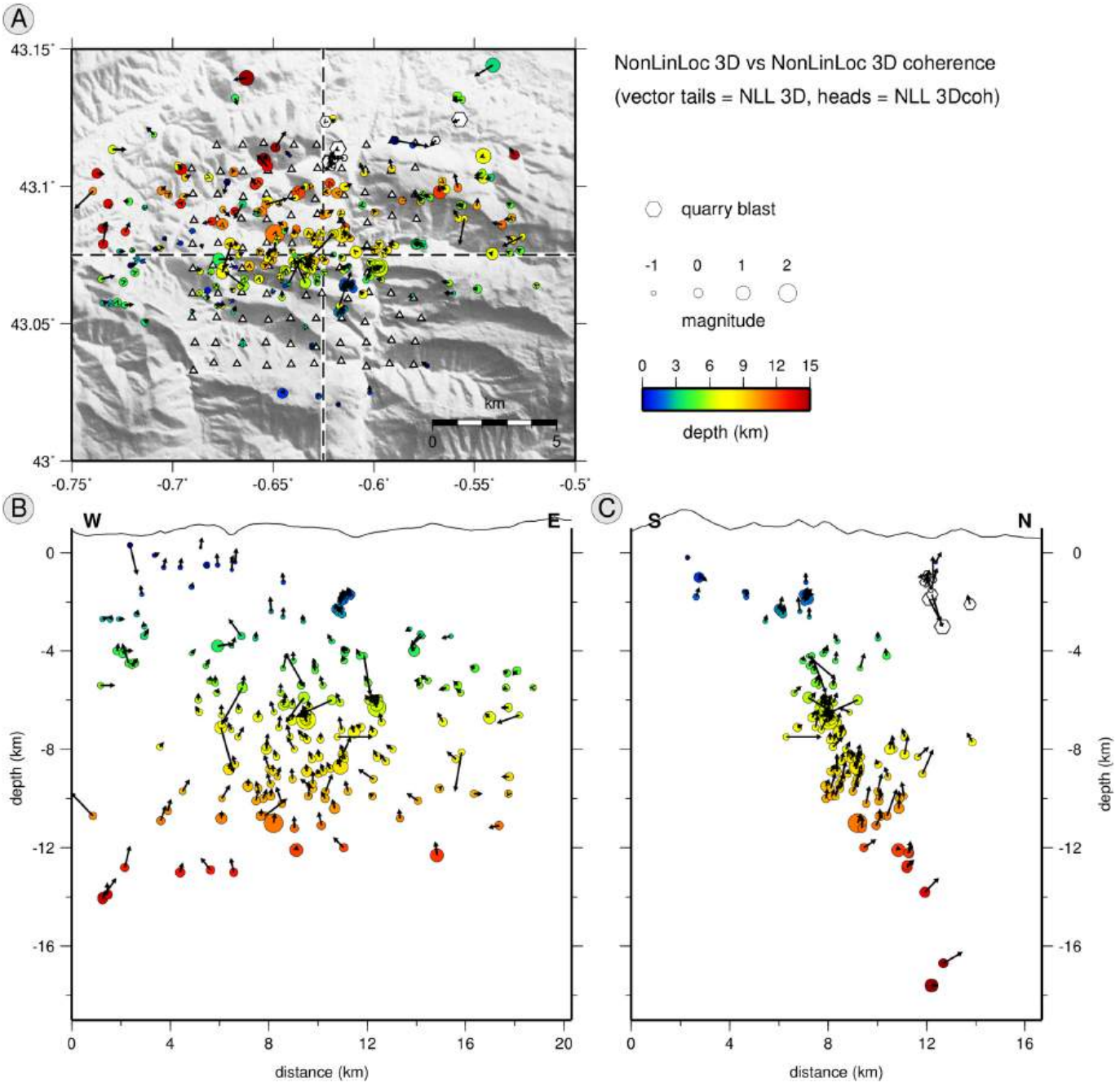

Fig. 9. Effect of source-specific station travel time corrections and inter-event waveform coherence on earthquake locations. a) Map showing the epicenters (colored circles) located in the 1D model, stations (white triangles), and relocation vectors (black arrows), pointing from 3D to 3D SST-Coherence locations. The size of the circles scales with the magnitude and the colour code indicate the depth of the events. White hexagons are identified quarry blasts. The dashed lines show the positions of the *E*-W and N-S cross-sections. b) E-W vertical cross-section showing the hypocenters and relocation vectors, projected on the vertical plane. c) same as b) but for the N-S vertical cross-section. In both cross-sections, the scale is the same for distance and depth, and the projection width is ±3 km.

deep in the 1D model, the 3D locations tend to be shallower, whereas for those located less than 8 km deep, the 3D locations tend to move to greater depths. This simple and coherent pattern can be explained by the effect of the low-velocity sedimentary cover, which is not accounted for in the 1D model. We also note that 3D hypocenters relocated at superficial levels (depths less than 4 km) tend to follow the detachment level at the base of the sedimentary cover, whereas deeper earthquakes tend to concentrate along a single north-dipping fault (the CBNF) that can be followed to a depth of around 16 km, which presumably corresponds to the brittle-ductile transition. Consequently, these observations suggest that 1D hypocenter locations may be significantly biased, even if the seismicity is recorded by a dense array deployed on top of it. For robust and precise earthquake locations, using a high-resolution 3D model is thus mandatory.

5.3. *Relocations using source-specific station terms and inter-event waveform similarity*

We now relocate the complete catalog using 3D source-specific station travel-time (SSST) corrections and inter-event waveform coherence (Coherence). For a detailed description of this refined location procedure the reader is referred to Lomax and Savvaidis (2021). In a first step, the algorithm estimates the SSST corrections for each source-event path. A Gaussian spatial smoothing is applied to these corrections, progressively and iteratively reducing the smoothing length of the smoothing kernel, following a similar approach as in Lin and Shearer (2005). In a second step, the algorithm exploits waveform similarity in order to improve relative location accuracy. The idea is that if two earthquakes have similar waveforms at a given station, then this implies that their relative distance is small compared to the dominant seismic wavelength.

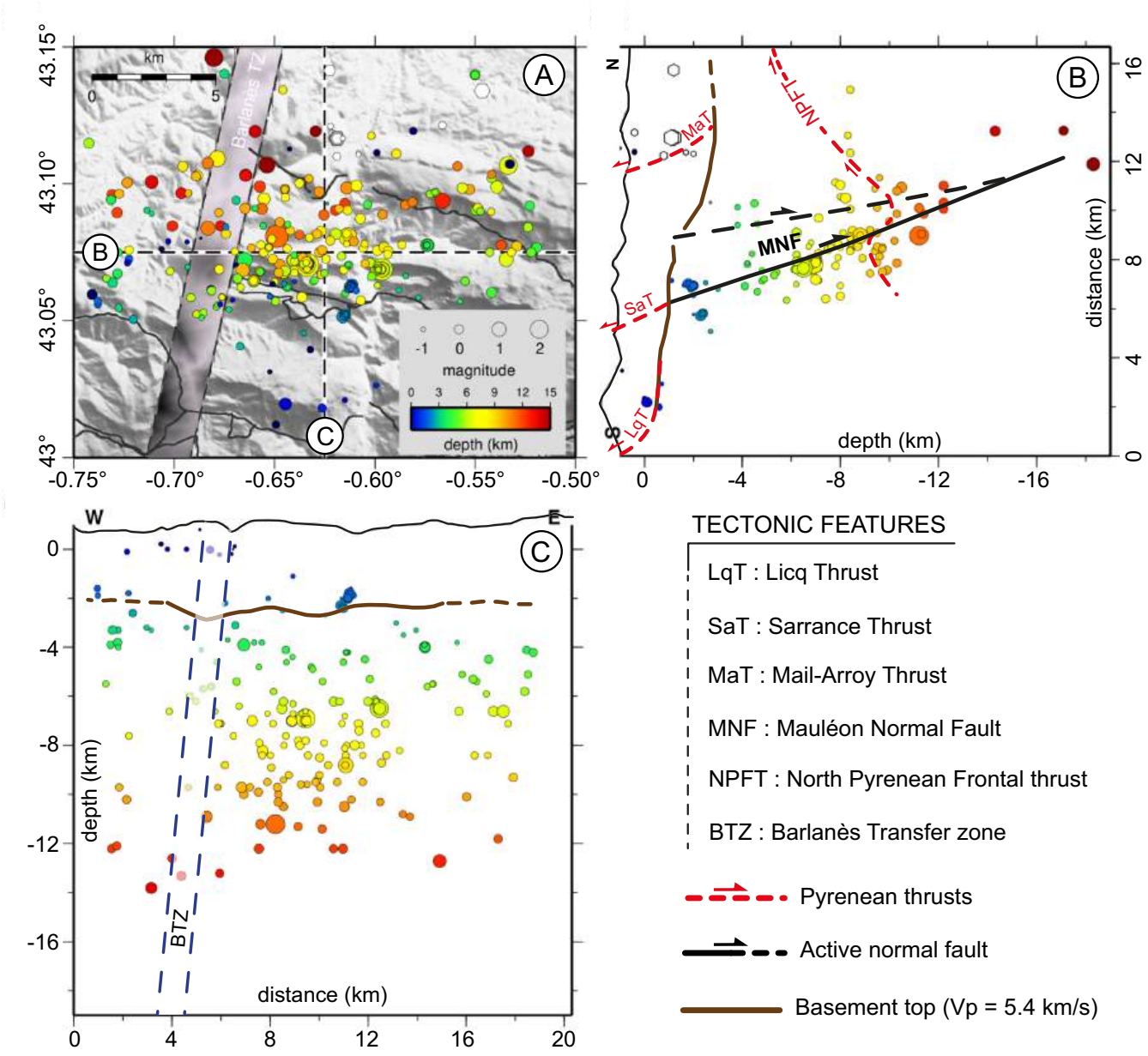

Fig. 10. Final hypocenter locations obtained with the NLL-SSST-coherence method in the 3D model. (a) Map view, with event size proportional to magnitude, and colour related to focal depth. White hexagons are identified quarry blasts. Dashed lines correspond to the positions of the cross-sections. (b) S/N cross-section. (c) E/W cross-section. In both cross-sections, the scale is the same for distance and depth, and the projection width is ±3 km.

The waveform coherence between two events is quantified by the maximum normalized cross-correlation coefficient obtained by considering all the stations. The cross-correlations were computed over a 10 s time window that contains both P and S arrivals after filtering the records between 4 and 20 Hz. The rather high upper frequency limit is justified by the small magnitudes of the events recorded during the Arette experiment. For each target event, we compute a normalized stack of the pdfs corresponding to the events which have a normalized correlation coefficient above 0.5. This allows a precise relative location of events that belong to the same seismicity cluster.

Fig. 9 shows the variations in hypocenter locations after applying the NLL-SSST-Coherence location procedure. For most events, the relocation vectors are very small. This suggests that the SSST corrections have little effect on hypocenter locations, presumably because the 3D effects are already properly accounted for in the travel time tables computed in the tomographic model. Nevertheless, a number of events have their locations significantly impacted by accounting for waveform coherence, and are brought within small clusters of events with presumably similar waveforms.

Fig. 10 shows the final earthquake locations obtained with the NLL-

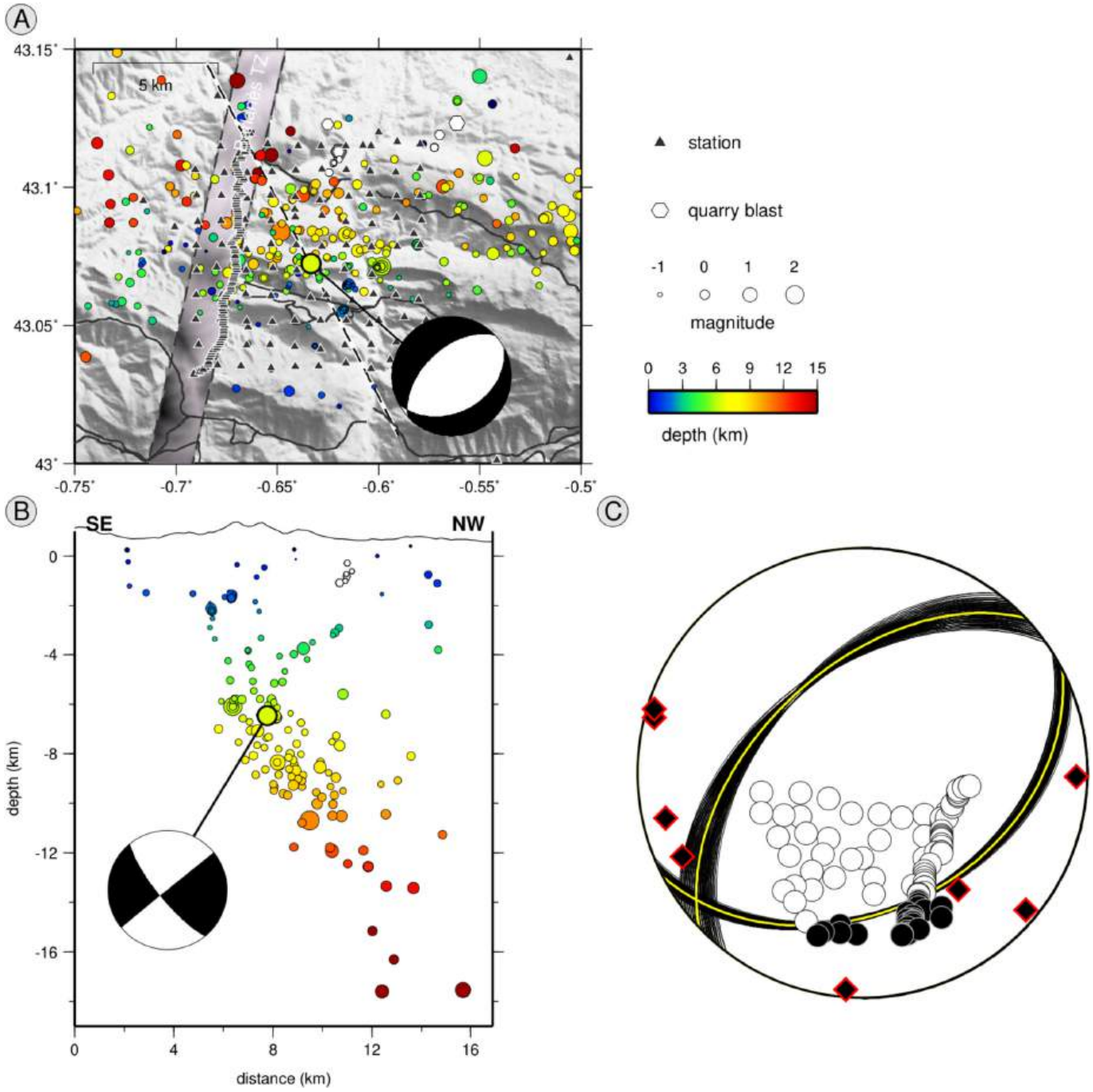

Fig. 11. Focal solution computed from P-wave polarities for the strongest event of the catalog (2022.06.07–09:31, M_L = 2.1). (A) Map view, with event size proportional to magnitude, and colour related to focal depth. White hexagons are identified quarry blasts. The SE/NW oriented dashed line corresponds to the position of the cross-section B. (B) Cross-section perpendicular to the strike of the fault planes. (C) Details of the possible focal planes, and individual P-waves polarities. Yellow lines: preferred planes. Red-circled diamonds correspond to permanent stations of the RESIF-EPOS network. (For interpretation of the references to colour in this figure legend, the reader is referred to the web version of this article.)

SSST-Coherence method, in map view and along two vertical cross-sections oriented E-W and N-S. On the N-S cross-section (Fig. 10B), we can clearly see that the seismicity roughly aligns with the north-dipping fault imaged by LET. This fault maintains an almost constant dip throughout the upper crust. It does not seem to be rooting in a flat detachment level that typically marks the transition from brittle to ductile regimes. Seismicity is unevenly distributed on the fault, forming small clusters located at varying depths, and within a damaged zone several hundred meters wide surrounding the main fault. The distribution of seismicity and the tomographic model also suggest subsidiary deformation, forming a horsetail mesh in the hanging wall beneath the sedimentary cover. Such deformation, common in competent low-

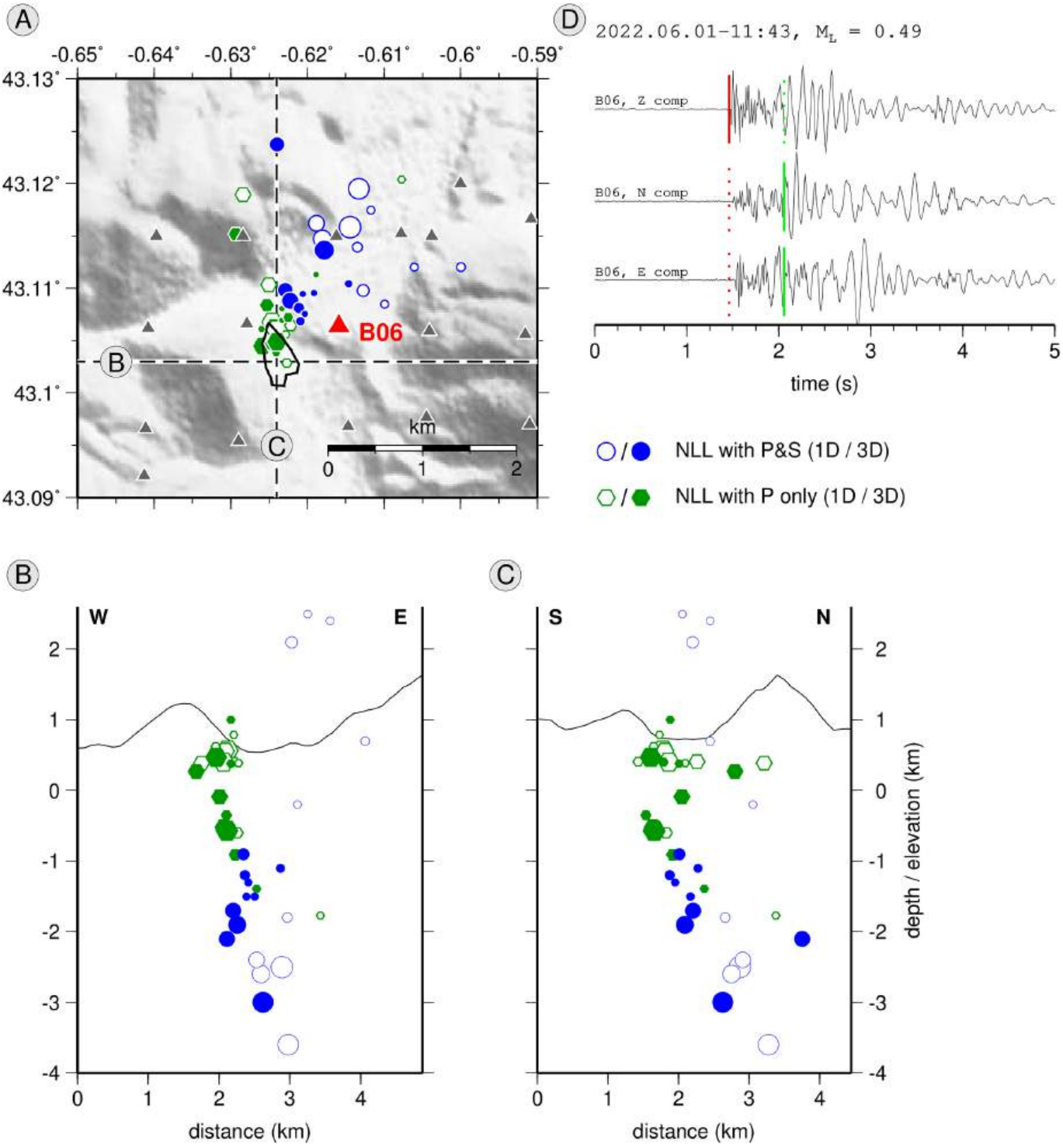

Fig. 12. Relocation of artificial events from the Asasp-Arros limestone quarry. (A) Map view. Dashed lines correspond to the positions of the cross-sections. The plain line outlines the quarrying zone. Triangles are seismological stations. Blue circles are locations performed with PhaseNet P and S picks, and green hexagons with P only. Empty symbols correspond to the 1D case, full symbols to the 3D case. (B) S/N cross-section. (C) E/W cross-section. (D) Example of automatic P and S picks performed with PhaseNet on a shot recorded at station B06, 1 km from the quarry. (For interpretation of the references to colour in this figure legend, the reader is referred to the web version of this article.)

porosity rocks like metamorphosed basement, can produce permeable conduits that can concentrate topographically-driven fluid circulation (Sibson, 2000). If this interpretation is correct, then our results imply a high-permeability flow system extending to at least 12 km depth, potentially affecting the entire upper crust. Shallow seismicity located beneath the Mail Arrouy Thrust (MaT), represented with open hexagons, is actually related to quarry blasts (see below). On the E-W section, despite the continuous expression of the main north-dipping fault, we observe a marked contrast in the distribution of seismicity across the BTZ. To the west of the BTZ, where recent tomographic studies revealed the presence of serpentinized mantle (Lehujeur et al., 2021), earthquakes are fewer and more sparsely distributed. This difference suggests that part of the deformation west of the BTZ might be accommodated by aseismic slip in the weak serpentinized mantle.

5.4. Focal mechanisms

The low magnitudes of the events recorded during the experiment imposed first-motion polarities as the *defacto* choice for calculating focal mechanisms. We therefore used the FOCMEC package (Snoke, 2003), applied to the first motion of P-waves. A first difficulty was to succeed in reading polarities on the Stryde accelerometers, which was generally only possible after integrating twice to switch from acceleration to displacement, and only for very energetic signals. In addition to these reading problems, determining focal mechanisms proved to be a difficult task due to the malfunction of many of the vertical components of the instruments, the small aperture of the network, and the relatively large depths of the earthquakes relative to this aperture. Fig. 11C illustrates this difficulty. If we were able to obtain the focal mechanism of the strongest event in the catalog (magnitude 2.1) with satisfactory accuracy, it was largely thanks to readings from permanent monitoring stations located several tens of km from the hypocenter. Without this control from remote stations, and therefore for the majority of earthquakes too small to generate impulsive signals at reasonable distances, it was impossible to determine focal planes with a good degree of confidence. Nevertheless, the focal solution of this strongest event fits perfectly into the structural scheme revealed by the seismicity. The faulting is undoubtedly normal, as it should be for the CBNF, and projection of the seismicity onto a plane perpendicular to the strike (62°) of the focal planes allows good discrimination between the two (Fig. 11B) via the dip angle (39°).

6. Discussion

6.1. Quarry blasts: discrimination, S phase picks, and locations

The preliminary identification and elimination of quarry blasts from seismicity catalogs is crucial for the identification of active faults and the assessment of seismic hazard. In our preliminary catalog, we identified several shallow events located beneath the Mail Arrouy thrust, which, after visual inspection, turned out to be quarry blasts. Fig. 12D shows a typical record of a quarry blast, in this case a shot in the Asasp-Arros quarry recorded by nearby station B06. A strong surface wave train arrives about 0.5 s after the P wave, instead of the more impulsive S wave usually observed on natural earthquake records. Nevertheless, although PhaseNet was only trained to detect and pick P and S waves on (Californian) earthquakes, it detected and picked surface wave arrivals from quarry blasts, wrongly identifying them as S waves. The overestimated S—P delays lead to overestimated hypocentral depths. The effect of the poor quality of S picks on this type of event becomes clear when we compare 1D and 3D NLL locations using either P and S picks or P picks only (Fig. 12A-C). The 1D locations (open blue circles) using both P and S picks show epicenter locations offset by about 1 km to the north of the quarry (black solid line in Fig. 12), and with poorly resolved hypocentral depths, ranging from over 1 km above the surface down to 3.7 km depth. The 3D locations (filled blue circles) are slightly improved, with epicenters moved closer to the quarry, and hypocentral depths regrouped between 1 and 3 km depth. After discarding the S wave picks, the 1D locations (open green hexagons) move to a position much closer to the quarry, both vertically and laterally. The 3D locations (filled green hexagons) move even closer to the quarry. These simple observations highlight the detrimental effect of poor S picks for the location of quarry blasts, a conclusion already drawn by Gomberg et al. (1990) for natural earthquakes. We note that the catalog of pyrenean seismicity also contains shallow events beneath the Mail Arrouy (Fig. 3), which probably correspond to quarry blasts that should be removed from the catalog.

6.2. Influence of the 3D velocity model and waveform coherence on earthquake location

Fig. 7 shows that, for most events, statistical location errors are small, of the order of a few hundred meters, and that the location biases resulting from using an inadequate velocity model can be considerably larger. This suggests that the statistical error locations derived by the Monte-Carlo search should not be taken at face value. Nevertheless, it is interesting to explore more systematically the distribution of location errors and 1D—3D relocation vectors. Fig. 13A-B shows the horizontal and vertical 3D relocation distances as a function of the number of picks. Events with a small number of picks (typically less than 10) systematically show significant (up to several tens of km) vertical and horizontal differences between 1D and 3D locations. A similar trend can be seen in Figs. 13C-D, showing horizontal and vertical errors, respectively, as a function of the number of picks. These events correspond to very low magnitude earthquakes recorded by a very small number of stations, which means that the position of the epicenter and depth of the hypocenter are poorly constrained. Several events have large 3D relocation vectors and/or large location errors, even though they were located with a very large number of P and S picks (up to several hundreds). These events are well recorded by a large number of stations, but because of their great distance from the array, they are also poorly located. For events located outside the array, but close to it, the 3D locations are very good. Note that, in general, the change in hypocenter location is greater horizontally than vertically (Fig. 13A, B).

To first order, the number of picks seems to be a good indicator of the quality of the earthquake locations. We found no correlation between the azimuthal gap and location errors, except when the latter is greater than 320°, i.e. for events located far from the array. We also observe no clear correlation between the travel time rms and the number of picks, except when this number is low (typically less than 10). This is simply due to the fact that it is easier to find source parameters that provide an excellent fit to the observed travel times when the number of picks is small.

These results suggest that in our experiment the accuracy of hypocenter locations is remarkable, particularly for events located within the array and which have been well recorded by a large number of stations. Fig. 14 presents a statistical analysis of travel time residuals, horizontal, and vertical errors resulting from the 1D, 3D, and 3D SST-Coherence location methods, respectively. Histograms of travel time residuals (Fig. 14A) shows that for most events, the travel time residuals are quite small, of the order of 0.05 s, and follow very similar distributions. However, the SSST-Coherence method provides travel time residuals of less than 0.05 s for about 25 % of the events. These extremely small residuals are probably the result of improved location of events belonging to waveform-coherent clusters. Horizontal and vertical errors show similar behaviors. The 3D locations show slightly reduced travel time residuals as well as horizontal and vertical errors compared with 1D locations. Finally, we note that horizontal errors are larger than vertical ones. In general, these errors are of the order of a few hundreds meters, about an order of magnitude smaller than typical statistical errors reported in seismicity studies based on coarser permanent regional networks (e.g., Husen et al., 2003; Theunissen et al., 2017).

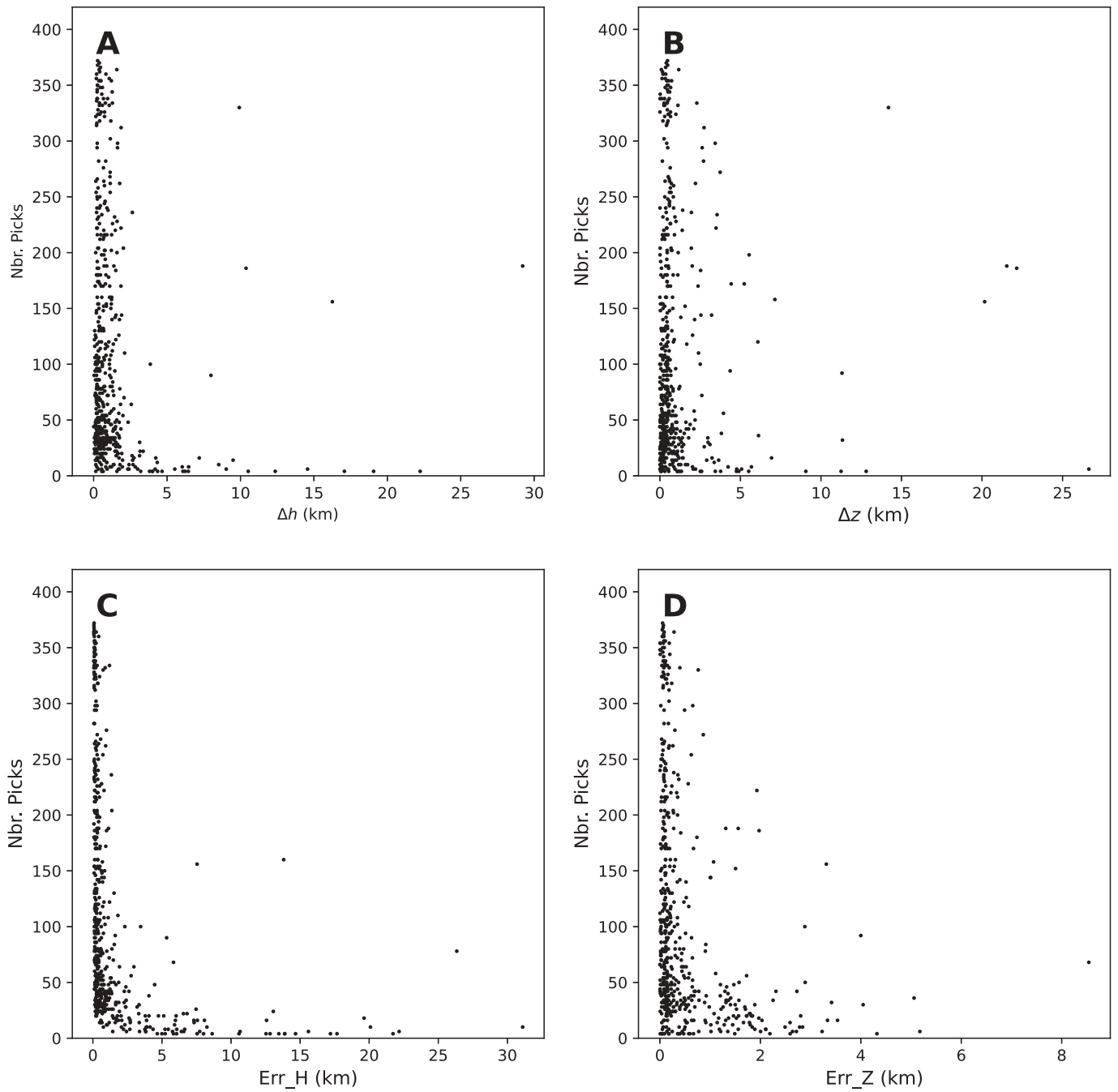

Fig. 13. Influence of the 3D velocity model on hypocenter locations. Horizontal (A) and vertical (B) distance between 1D and 3D hypocenter locations versus number of picks. Horizontal (C) and vertical (D) statistical errors in the 3D model versus number of picks.

6.3. Active faults and implications for seismic hazard

An important issue for seismic hazard is related to the size and segmentation of active faults. In the continental crust, the seismogenic zone is confined to the top 10–20 km, depending on the depth of the brittle-ductile transition. The lateral dimensions of active faults is variable and poorly constrained in complex tectonic settings such as the Pyrenees. However, it is a key factor in determining the size of the largest earthquakes that can strike a given region.

Our results point to a main active fault, the Chaînons Béarnais Normal Fault (CBNF), in the Chaînons Béarnais region. This fault, which affects the Hercyninan basement, appears continuous across the Barlanès Transfer Zone, and may be connected to the Sarrance thrust (SaT) which crosses the sedimentary cover and reaches the surface. However, the seismicity appears to be sparser and more diffuse to the west of the Barlanès Transfer Zone, a segment of the fault on which the 1967 Arette earthquake probably occurred. In contrast, the segment of the fault east of the CBNF has not experienced any earthquake with magnitude larger than 4 during the last decades. This may suggest that the continuous but small intensity seismicity may prevent large stress accumulations on that fault segment.

Several earthquakes are located close to the detachment, in particular to the south of the CBNF, suggesting that part of the deformation may also be accommodated along this weak interface, which connects to the Licq thrust (LqT) at the surface. We do not find any evidence of an active, deeply rooted, fault beneath the Mail Arrouy, as proposed by several authors (Alasset and Meghraoui, 2005; Dubos-Sallée et al., 2007; Lacan and Ortuño, 2012). Search for surface expression of active faults

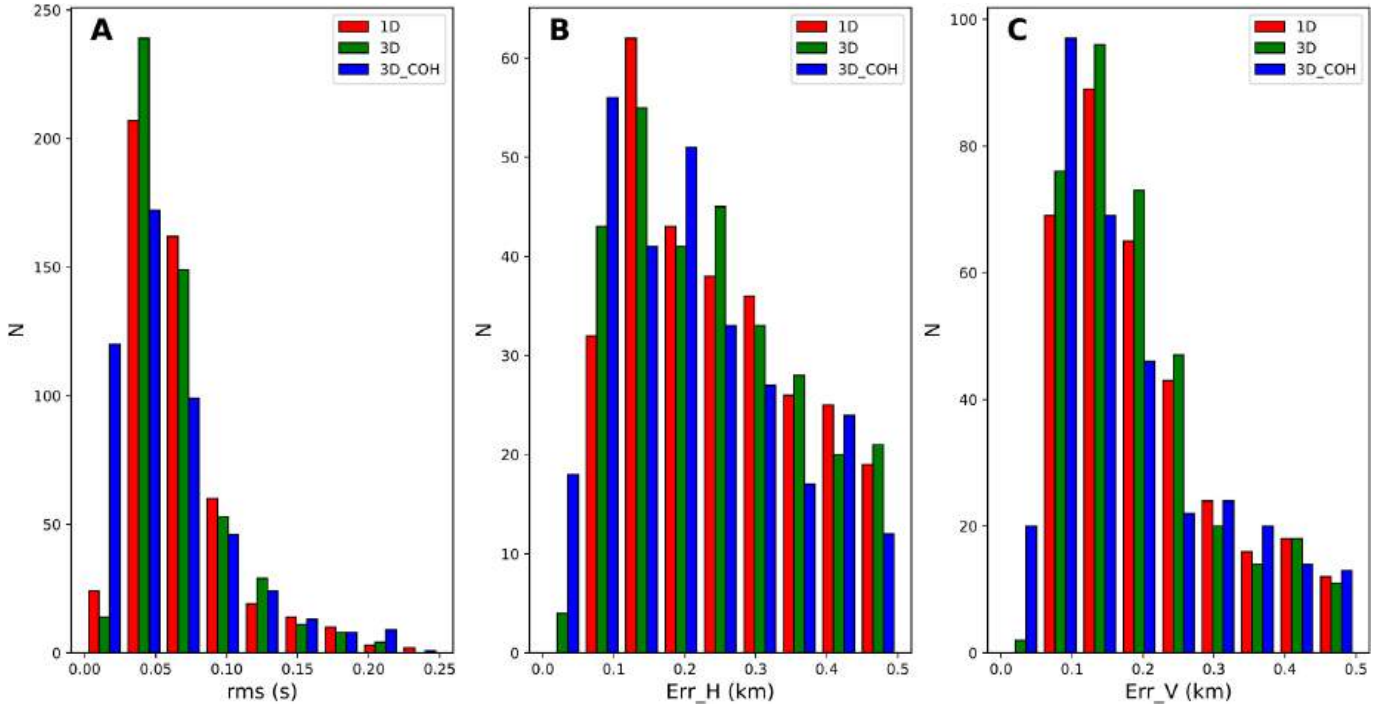

Fig. 14. Histograms of travel time residuals (A), horizontal (B), and vertical (C) errors derived from the 68 % confidence ellipsoid.

in this area should thus focus on the Licq and Sarrance thrusts.

The nature and origin of the deep fault affecting the basement - whether newly formed or inherited - are still uncertain and certainly require further research. Nevertheless, it is interesting to note that the CBNF coincides with a steep variation of crustal thickness, between the thick crustal root of the Axial Zone and the thin North Pyrenean Zone crust (e.g., Chevrot et al., 2022). Recent thermochronological data revealed a Miocene phase of rapid exhumation between 11 and 9 Ma in the Axial Zone, followed by a post-orogenic phase of exhumation that started around 10 Ma (Fillon et al., 2020). The regional isostatic compensation of the post-orogenic rebound (Lacan and Ortuño, 2012; Genti et al., 2016) could therefore explain normal faulting localized on the CBNF. Similar conclusions were drawn by Lescoutre et al. in their analysis of the seismicity in the western Pyrenees, beneath the Mauléon basin.

7. Conclusions

Our study demonstrates that single-component accelerometric nodes can be recombined to produce three-component records of sufficient quality to record local seismicity in the 2–20 Hz frequency range. Although PhaseNet, a deep neural network, has been trained on broadband earthquake recordings in California, it is capable of successfully detecting and picking P and S waves of regional earthquakes at distances ranging from less than one kilometer to several tens of kilometers on accelerometric node recordings. The small inter-station spacing of approximately 1 km in our experiment enabled us to detect local events with magnitudes as small as around −1. Such small events could not have been detected or localized with the permanent network, which has a typical inter-station spacing of a few tens of kilometers. For many of these small events, multiple stations within an epicentral distance less than the hypocentral depth reported both P and S picks, allowing precise determination of the source parameters, particularly hypocentral depth. These events can therefore be utilized for local earthquake tomography, yielding crustal models with a resolution of a few hundred meters, approaching the resolution of active source imaging. Tomographic images reveal folds and thrusts in the sedimentary cover, in excellent agreement with surface geology, as well as a deeply fractured Hercynian basement. A principal north-dipping fault is clearly delineated, extending from the base of the sedimentary cover to approximately 16 km depth, along which the majority of deep seismicity aligns. These findings present promising avenues for crustal imaging and characterization of active faults using dense deployments of affordable and easily deployable sensors.

CRediT authorship contribution statement

Sébastien Chevrot: Writing – review & editing, Writing – original draft, Validation, Supervision, Project administration, Methodology, Investigation, Funding acquisition, Data curation, Conceptualization. **Matthieu Sylvander:** Writing – review & editing, Writing – original draft, Validation, Supervision, Project administration, Methodology, Investigation, Funding acquisition, Data curation, Conceptualization. **Nicolas Saspiturry:** Writing – review & editing, Writing – original draft, Validation, Supervision, Project administration, Methodology, Investigation, Funding acquisition, Data curation, Conceptualization. **Amine Ourabah:** Writing – review & editing, Writing – original draft, Validation, Supervision, Project administration, Methodology, Investigation, Funding acquisition, Data curation, Conceptualization. **Sébastien Benahmed:** Writing – review & editing, Writing – original draft, Validation, Supervision, Project administration, Methodology, Investigation, Funding acquisition, Data curation, Conceptualization. **Benoît Derode:** Writing – review & editing, Writing – original draft, Validation, Supervision, Project administration, Methodology, Investigation, Funding acquisition, Data curation, Conceptualization. **Frank Grimaud:** Writing – review & editing, Writing – original draft, Validation, Supervision, Project administration, Methodology, Investigation, Funding acquisition, Data curation, Conceptualization. **Jean Letort:** Writing – review & editing, Writing – original draft, Validation, Supervision, Project administration, Methodology, Investigation, Funding acquisition, Data curation, Conceptualization. **Hélène Pauchet:** Writing – review & editing, Writing – original draft, Validation, Supervision, Project administration, Methodology, Investigation, Funding acquisition, Data curation, Conceptualization. **Guy Sénéchal:** Writing – review

& editing, Writing – original draft, Validation, Supervision, Project administration, Methodology, Investigation, Funding acquisition, Data curation, Conceptualization. **Antonio Villaseñor:** Writing – review & editing, Writing – original draft, Validation, Supervision, Project administration, Methodology, Investigation, Funding acquisition, Data curation, Conceptualization. **Jean-Baptiste Ammirati:** Writing – review & editing, Writing – original draft, Validation, Supervision, Project administration, Methodology, Investigation, Funding acquisition, Data curation, Conceptualization.

Declaration of competing interest

The authors declare that they have no known competing financial interests or personal relationships that could have appeared to influence the work reported in this paper.

Data availability

Data will be made available on request.

Acknowledgments

AV acknowledges funding from the Severo Ochoa Center of Excellence accreditation CEX2019-000928-S to Institute of Marine Sciences (ICM- CSIC). SC acknowledges funding from the Institut Carnot ISIForE.

Appendix A. Supplementary data

Supplementary data to this article can be found online at https://doi.org/10.1016/j.tecto.2024.230531.

References

Alasset, P.-J., Meghraoui, M., 2005, November. Active faulting in the western Pyrénées (France): Paleoseismic evidence for late Holocene ruptures. Tectonophysics 409 (1–4), 39–54. https://doi.org/10.1016/j.tecto.2005.08.019.

Ammirati, J.-B., Villaseñor, A., Chevrot, S., Easton, G., Lehujeur, M., Ruiz, S., Flores, M. C., 2022, Apr. Automated earthquake detection and local travel time tomography in the South-Central Andes (32–35°S): Implications for regional tectonics. J. Geophys. Res. Solid Earth 127 (4). https://doi.org/10.1029/2022jb024097.

Angrand, P., Ford, M., Watts, A.B., 2018. Lateral variations in foreland flexure of a rifted continental margin: the Aquitaine Basin (SW France). Tectonics 37, 430–449.

Angrand, P., Mouthereau, F., Masini, E., Asti, R., 2020, July. A reconstruction of Iberia accounting for Western Tethys–North Atlantic kinematics since the late-Permian–Triassic. Solid Earth 11 (4), 1313–1332. https://doi.org/10.5194/se-11-1313-2020.

Benz, H.M., Chouet, B.A., Dawson, P.B., Lahr, J.C., Page, R.A., Hole, J.A., 1996, April. Three-dimensional P and S wave velocity structure of Redoubt Volcano, Alaska. J. Geophys. Res. Solid Earth 101 (B4), 8111–8128. https://doi.org/10.1029/95jb03046.

Canérot, J., 1988. Manifestations de l'halocinèse dans les chaînons béarnais (Zone Nord-Pyrénéenne) au Crétacé inférieur. Comptes Rendus de l'Académi. des Sci. Série 2, Mécanique, Physique, Chimie, Sciences de l'univers Sci. Terre 306 (15), 1099–1102.

Canérot, J., 2017. The pull apart-type Tardets-Mauléon basin, a key to understand the formation of the Pyrenees. Bull. de la Soci. Géol. France 188 (6), 35. https://doi.org/10.1051/bsgf/2017198.

Canérot, J., Hudec, M.R., Rockenbauch, K., 2005. Mesozoic diapirism in the Pyrenean orogen: Salt tectonics on a transform plate boundary. AAPG Bull. 89 (2), 211–229.

Chevrot, S., Sylvander, M., Delouis, B., 2011. A preliminary catalogue of moment tensors for the Pyrenees. Tectonophysics 510, 239–251.

Chevrot, S., Sylvander, M., Villaseñor, A., Díaz, J., Stehly, L., Boué, P., Vidal, O., 2022. Passive imaging of collisional orogens: a review of a decade of geophysical studies in the Pyrénées. BSGF - Earth Sciences Bulletin 193, 1. https://doi.org/10.1051/bsgf/2021049.

Choukroune, P., 1976, October. Strain patterns in the Pyrenean Chain. Philosoph. Trans. Royal Soci. London Series A, Mathemat. Phys. Sci. 283 (1312), 271–280. https://doi.org/10.1098/rsta.1976.0084.

Derode, B., Gounon, A., Letort, J., Sylvander, M., Rigo, A., Benahmed, S., Santamaria, A., 2023, April. Fluid-driven seismic swarms in the Gripp valley (Haute-Pyrénées, France). Geophys. J. Int. 234 (3), 1903–1915. https://doi.org/10.1093/gji/ggad175.

Dieulangard, D., Popham, M., Grant, C., O'Connell, K., Ourabah, A., Einchcomb, C., 2022, January. Land Seismic Recording Systems in a Changing World — a 2021 Review. First Break 40 (1), 59–65. https://doi.org/10.3997/1365-2397.fb2022004.

Dubos-Sallée, N., Nivière, B., Lacan, P., Hervouët, Y., 2007, October. A structural model for the seismicity of the Arudy (1980) epeicentral area (Western Pyrenees, France). Geophys. J. Int. 171 (1), 259–270. https://doi.org/10.1111/j.1365-246x.2007.03499.x.

Duverger, C., Mazet-Roux, G., Bollinger, L., Guilhem Trilla, A., Vallage, A., Hernandez, B., Cansi, Y., 2021. A decade of seismicity in metropolitan France (2010–2019): the Cea/ldg methodologies and observations. BSGF - Earth Sci. Bull. 192, 25. Retrieved from. https://doi.org/10.1051/bsgf/2021014.

Espurt, N., Angrand, P., Teixell, A., Labaume, P., Ford, M., de Saint Blanquat, M., Chevrot, S., 2019, August. Crustal-scale balanced cross-section and restorations of the Central Pyrenean belt (Nestes-Cinca transect): Highlighting the structural control of Variscan belt and Permian-Mesozoic rift systems on mountain building. Tectonophysics 764, 25–45. https://doi.org/10.1016/j.tecto.2019.04.026.

Fillon, C., Mouthereau, F., Calassou, S., Pik, R., Bellahsen, N., Gautheron, C., van der Beek, P., 2020, December. Post-orogenic exhumation in the western Pyrenees: evidence for extension driven by pre-orogenic inheritance. J. Geol. Soc. Lond. 178 (2). https://doi.org/10.1144/jgs2020-079.

García, J.E., Fernández-Prieto, L.M., Villaseñor, A., Sanz, V., Ammirati, J.-B., Díaz Suárez, E.A., García, C., 2022, July. Performance of Deep Learning Pickers in Routine Network Processing applications. Seismol. Res. Lett. 93 (5), 2529–2542. https://doi.org/10.1785/0220210323.

Genti, M., Chery, J., Vernant, P., Rigo, A., 2016, March. Impact of gravity forces and topography denudation on normal faulting in Central–Western Pyrenees: Insights from 2D numerical models. Compt. Rendus Geosci. 348 (3–4), 173–183. https://doi.org/10.1016/j.crte.2015.08.004.

Gomberg, J.S., Shedlock, K.M., Roecker, S.W., 1990, December. The effect of S-wave arrival times on the accuracy of hypocenter estimation. Bull. Seismol. Soc. Am. 80 (6A), 1605–1628. https://doi.org/10.1785/bssa08006a1605.

Husen, S., Kissling, E., Deichmann, N., Wiemer, S., Giardini, D., Baer, M., 2003, February. Probabilistic earthquake location in complex three-dimensional velocity models: Application to Switzerland. J. Geophys. Res. Solid Earth 108 (B2). https://doi.org/10.1029/2002jb001778.

Issautier, B., Saspiturry, N., Serrano, O., 2020, August. Role of structural inheritance and salt tectonics in the formation of pseudosymmetric continental rifts on the european margin of the hyperextended Mauléon basin (early cretaceous Arzacq and Tartas Basins). Mar. Pet. Geol. 118, 104395. https://doi.org/10.1016/j.marpetgeo.2020.104395.

Issautier, B., Lasseur, E., Saspiturry, N., Angrand, P., Andrieu, S., Serrano, O., 2022, November. Onset of Iberian-European plate convergence: late cretaceous flexural response of a hot lithosphere (Aquitaine Basin, France). Tectonophysics 843, 229504. https://doi.org/10.1016/j.tecto.2022.229504.

James, V., Canérot, J., 1999. Diapirisme et structuration post-triasique des Pyrénées occidentales et de l'Aquitaine méridionale (France). Eclogae Geol. Helv. 92 (1), 63–72.

Jammes, S., Manatschal, G., Lavier, L., Masini, E., 2009. Tectonosedimentary evolution related to extreme crustal thinning ahead of a propagating ocean: example of the western Pyrenees. Tectonics 28. https://doi.org/10.1029/2008TC002406. TC4012.

Labaume, P., Teixell, A., 2020, June. Evolution of salt structures of the Pyrenean rift (Chaînons Béarnais, France): from hyper-extension to tectonic inversion. Tectonophysics 785, 228451. https://doi.org/10.1016/j.tecto.2020.228457051.

Lacan, P., Ortuño, M., 2012, September. Active Tectonics of the Pyrenees: a review. J. Iber. Geol. 38 (1). https://doi.org/10.5209/rev_jige.2012.v38.n1.39203.

Lagabrielle, Y., Labaume, P., de Saint Blanquat, M., 2010. Mantle exhumation, crustal denudation, and gravity tectonics during cretaceous rifting in the Pyrenean realm (SW Europe): Insights from the geological setting of the lherzolite bodies. Tectonics 29, TC4012.

Lagabrielle, Y., Asti, R., Duretz, T., Clerc, C., Fourcade, S., Teixell, A., Saspiturry, N., 2020, February. A review of cretaceous smooth-slopes extensional basins along the Iberia-Eurasia plate boundary: how pre-rift salt controls the modes of continental rifting and mantle exhumation. Earth Sci. Rev. 201, 103071. https://doi.org/10.1016/j.earscirev.2019.103071.

Lehujeur, M., Chevrot, S., 2020. Eikonal tomography using coherent surface waves extracted from ambient noise by iterative matched filtering - Application to the large-N Maupasacq array. J. Geophys. Res. 125, e2020JB019363. https://doi.org/10.1029/2020JB019363.

Lehujeur, M., Chevrot, S., Villaseñor, A., Masini, E., Saspiturry, N., Lescoutre, R., Sylvander, M., 2021. Three-dimensional shear velocity structure of the Mauléon and Arzacq Basins (Western Pyrenees). BSGF - Earth Sciences Bulletin 192, 47. https://doi.org/10.1051/bsgf/2021039.

Lescoutre, R., Manatschal, G., 2020. Role of rift-inheritance and segmentation for orogenic evolution: example from the Pyrenean-Cantabrian system. BSGF - Earth Sciences Bulletin 191, 18. https://doi.org/10.1051/bsgf/2020021.

Lescoutre, R., Tugend, J., Brune, S., Masini, E., Manatschal, G., 2019, October. Thermal Evolution of Asymmetric Hyperextended Magma-Poor Rift Systems: results from Numerical Modeling and Pyrenean Field Observations. Geochem. Geophys. Geosyst. 20 (10), 4567–4587. https://doi.org/10.1029/2019gc008600.

Lin, G., Shearer, P., 2005, April. Tests of relative earthquake location techniques using synthetic data. J. Geophys. Res. Solid Earth 110 (B4). https://doi.org/10.1029/2004jb003380.

Lomax, A., Savvaidis, A., 2021, December. High-precision earthquake location using source-specific station terms and inter-event waveform similarity. J. Geophys. Res. Solid Earth 127 (1). https://doi.org/10.1029/2021jb023190.

Lomax, A., Virieux, J., Volant, P., Berge-Thierry, C., 2000. Probabilistic earthquake location in 3D and layered models. In: Modern Approaches in Geophysics. Springer, Netherlands, pp. 101–134. https://doi.org/10.1007/978-94-015-9536-0_5.

Masini, E., Manatschal, G., Tugend, J., Mohn, G., Flament, J.M., 2014. The tectono-sedimentary evolution of a hyper-extended rift basin: the example of the Arzacq-Mauléon rift system (Western Pyrenees, France). Int. J. Earth Sci. 103, 1569–1596.

Masson, C., Mazzotti, S., Vernant, P., Doerflinger, E., 2019, November. Extracting small deformation beyond individual station precision from dense Global Navigation Satellite System (GNSS) networks in France and western europe. Solid Earth 10 (6), 1905–1920. https://doi.org/10.5194/se-10-1905-2019.

Mazzotti, S., Jomard, H., Masson, F., 2020. Processes and deformation rates generating seismicity in metropolitan France and conterminous Western Europe. BSGF - Earth Sciences Bulletin 191, 19. https://doi.org/10.1051/bsgf/2020019.

Mouthereau, F., Filleaudeau, P.Y., Vacherat, A., Pik, R., Lacombe, O., Fellin, M.G., Masini, E., 2014. Placing limits to shortening evolution in the Pyrenees: Role of margin architecture and implications for the Iberia/Europe convergence. Tectonics 33 (12), 2283–2314. https://doi.org/10.1002/2014TC003663.

Nocquet, J.-M., Sue, C., Walpersdorf, A., Tran, T., Lenôtre, N., Vernant, P., van der Beek, P.A., 2016, June. Present-day uplift of the western Alps. Sci. Rep. 6 (1). https://doi.org/10.1038/srep28404.

Olivet, J.L., 1996. La cinématique de la plaque Ibérique. Bull. Centres Rech. Explor. Prod. Elf-Aquitaine 20, 131–195.

Ortiz, A., Guillocheau, F., Lasseur, E., Briais, J., Robin, C., Serrano, O., Fillon, C., 2020, February. Sediment routing system and sink preservation during the post-orogenic evolution of a retro-foreland basin: the case example of the North Pyrenean (Aquitaine, Bay of Biscay) Basins. Mar. Pet. Geol. 112, 104085. https://doi.org/10.1016/j.marpetgeo.2019.104085.

Ortiz, A., Guillocheau, F., Robin, C., Lasseur, E., Briais, J., Fillon, C., 2022, March. Siliciclastic sediment volumes and rates of the North Pyrenean retro-foreland basin. Basin Res. 34 (4), 1421–1439. https://doi.org/10.1111/bre.12665.

Ourabah, A., Petronio, L., Affatato, A., Baradello, L., Goujon, N., Song, Z., 2021. Using 1C nodes in a 3C combination - benefits, and inconveniences. In: Nsg2021 27th european meeting of environmental and engineering geophysics. European Association of Geoscientists & Engineers. https://doi.org/10.3997/2214-4609.202120139.

Pauchet, H., Rigo, A., Rivera, L., Souriau, A., 1999, April. A detailed analysis of the February 1996 Aftershock sequence in the eastern Pyrenees, France. Geophys. J. Int. 137 (1), 107–127. https://doi.org/10.1046/j.1365-246x.1999.00776.x.

Pavlis, G.L., 1986. Appraising earthquake hypocenter location errors: a complete, practical approach for single-event locations. Bull. Seismol. Soc. Am. 76 (6), 1699–1717.

Podvin, P., Lecomte, I., 1991, April. Finite difference computation of travel-times in very contrasted velocity models: a massively parallel approach and its associated tools. Geophys. J. Int. 105 (1), 271–284. https://doi.org/10.1111/j.1365-246x.1991.tb03461.x.

Puigdefàbregas, C., Souquet, P., 1986, October. Tecto-sedimentary cycles and depositional sequences of the Mesozoic and Tertiary from the Pyrenees. Tectonophysics 129 (1–4), 173–203. https://doi.org/10.1016/0040-1951(86)90251-9.

Retailleau, L., Saurel, J.-M., Zhu, W., Satriano, C., Beroza, G.C., Issartel, S., Boissier, P., 2022, February. A wrapper to use a machine-learning-based algorithm for earthquake monitoring. Seismol. Res. Lett. 93 (3), 1673–1682. https://doi.org/10.1785/0220210279.

Rigo, A., Souriau, A., Dubos, N., Sylvander, M., Ponsolles, C., 2005. Analysis of the seismicity in the central part of the Pyrénées (France), and tectonic implications. J. Seismol. 9, 211–222.

Rigo, A., Vernant, P., Feigl, K.L., Goula, X., Khazaradze, G., Talaya, J., Sylvander, M., 2015, March. Present-day deformation of the Pyrenees revealed by GPS surveying and earthquake focal mechanisms until 2011. Geophys. J. Int. 201 (2), 947–964. https://doi.org/10.1093/gji/ggv052.

Saspiturry, N., Razin, P., Baudin, T., Serrano, O., Issautier, B., Lasseur, E., Leleu, S., 2019. Symmetry vs. asymmetry of a hyper-thinned rift: example of the Mauléon Basin (Western Pyrenees, France). Mar. Pet. Geol. 104, 86–105.

Saspiturry, N., Issautier, B., Razin, P., Baudin, T., Asti, R., Lagabrielle, Y., Duretz, T., 2021, January. Review of Iberia–eurasia plate-boundary basins: Role of sedimentary burial and salt tectonics during rifting and continental breakup. Basin Res. 33 (2), 1626–1661. https://doi.org/10.1111/bre.12529.

Saspiturry, N., Allanic, C., Serrano, O., Courrioux, G., Baudin, T., Le Bayon, B., Issautier, B., 2022, March. Upper lithospheric transfer zones driving the non-cylindricity of the West-Pyrenean orogenic prism (Mauléon hyperextended basin). J. Struct. Geol. 156, 104535. https://doi.org/10.1016/j.jsg.2022.104535.

Saspiturry, N., Allanic, C., Aurélie, P., 2024, July. Serpentinization and magmatic distribution in a hyperextended rift suture: Implication for natural hydrogen exploration (Mauléon basin, pyrenees). Tectonics 43. https://doi.org/10.1029/2024TC008385.

Schulte, S.M., Mooney, W.D., 2005, June. An updated global earthquake catalogue for stable continental regions: reassessing the correlation with ancient rifts. Geophys. J. Int. 161 (3), 707–721. https://doi.org/10.1111/j.1365-246x.2005.02554.x.

Sibson, R.H., 2000, April. Fluid involvement in normal faulting. J. Geodyn. 29 (3–5), 469–499. https://doi.org/10.1016/s0264-3707(99)00042-3.

Snoke, J., 2003. 85.12 focmec: Focal mechanism determinations. Int. Geophys. 81, 1629–1630. https://doi.org/10.1016/S0074-6142(03)80291-7.

Sykes, L.R., 1978, November. Intraplate seismicity, reactivation of preexisting zones of weakness, alkaline magmatism, and other tectonism postdating continental fragmentation. Rev. Geophys. 16 (4), 621–688. https://doi.org/10.1029/rg016i004p00621.

Sylvander, M., Rigo, A., Sénéchal, G., Battaglia, J., Benahmed, S., Calvet, M., Pauchet, H., 2021. Seismicity patterns in southwestern France. Compt. Rendus Géosci. 353 (S1), 79–104.

Tarantola, A., Valette, B., 1982. Inverse problems = Quest for information. J. Geophys. 50, 159–170.

Teixell, A., 1998. Crustal structure and orogenic material budget in the west Central Pyrenees. Tectonics 3, 395–406.

Teixell, A., Labaume, P., Lagabrielle, Y., 2016. The crustal evolution of the west-Central Pyrenees revisited: Inferences from a new kinematic scenario. Compt. Rendus Geosci. 348 (3–4), 257–267.

Theunissen, T., Chevrot, S., Sylvander, M., Monteiller, V., Calvet, M., Villaseñor, A., Grimaud, F., 2017, October. Absolute earthquake locations using 3-D versus 1-D velocity models below a local seismic network: example from the Pyrenees. Geophys. J. Int. 212 (3), 1806–1828. https://doi.org/10.1093/gji/ggx472.

Thurber, C.H., 1992, December. Hypocenter-velocity structure coupling in local earthquake tomography. Phys. Earth Planet. Inter. 75 (1–3), 55–62. https://doi.org/10.1016/0031-9201(92)90117-e.

Tryggvason, A., Rognvaldsson, S.T., Flovenz, O.G., 2002, December. Three-dimensional imaging of the P- and S-wave velocity structure and earthquake locations beneath Southwest Iceland. Geophys. J. Int. 151 (3), 848–866. https://doi.org/10.1046/j.1365-246x.2002.01812.x.

Wang, Y., Chevrot, S., Monteiller, V., Komatitsch, D., Mouthereau, F., Manatschal, G., Martin, R., 2016. The deep roots of the western Pyrenees revealed by full waveform inversion of teleseismic P waves. Geology 44 (6), 475–478.

Wittlinger, G., Herquel, G., Nakache, T., 1993, December. Earthquake location in strongly heterogeneous media. Geophys. J. Int. 115 (3), 759–777. https://doi.org/10.1111/j.1365-246x.1993.tb01491.x.

Zhang, M., Ellsworth, W.L., Beroza, G.C., 2019, September. Rapid earth-quake association and location. Seismol. Res. Lett. 90 (6), 2276–2284. https://doi.org/10.1785/0220190052.

Zhu, W., Beroza, G.C., 2019, October. Phasenet: A deep-neural-network-based seismic arrival time picking method. Geophys. J. Int. https://doi.org/10.1093/gji/ggy423.